Contents lists available at ScienceDirect

Surfaces and Interfaces

journal homepage: www.sciencedirect.com/journal/surfaces-and-interfaces



Enhancing hydrogen and ethanol gas sensing responses of CdO-ZnO heterostructure through ion irradiation

Arkaprava Das ^{a,*} [©], Peter Krüger ^b [©], Shuja Bashir Malik ^c [©], Juan Casanova-Chafer ^a [©], Fatima Ezahra Annanouch ^c [©], Ewa Partyka-Jankowska ^d [©], Marcin Zając ^d [©], Eduard Llobet ^c [©], Carla Bittencourt ^a [©]

- ^a Chimie des Interaction Plasma surface, University of Mons, Mons, Belgium
- ^b Materials Science Department, Graduate School of Engineering, Chiba University, Chiba, Japan
- ^c MINOS, Electronic Engineering Department, Universitat Rovira i Virgili, Spain
- d SOLARIS National Synchrotron Radiation Centre, Jagiellonian University, Krakow, Poland

ARTICLEINFO

Keywords: RF magnetron sputtering Irradiation Oxygen vacancies Gas sensing response X-ray absorption spectroscopy X-ray photoelectron spectroscopy Adsorption energy

ABSTRACT

This study investigates the modifications in the electronic excitation of $Cd_{0.4}Zn_{0.6}O$ (CZO) nanocomposite thin films resulting from irradiation with low-energy ions, with the aim of their application as active layers in hydrogen and ethanol gas sensing. The films were synthesized using radio frequency (RF) magnetron sputtering. Low kinetic energy (3 keV) ion irradiations using Oxygen and Argon ions at fluences of 1×10^{16} and 5×10^{17} ions/cm² were employed to optimize the electronic structure and enhance gas sensing responses. X-ray photoelectron and absorption spectroscopy demonstrated increased oxygen vacancy (V_O) concentration with irradiation. The higher nuclear energy loss for Ar ions led to the creation of more cationic vacancies. For both hydrogen and ethanol gas, the increased V_O concentration improved the gas sensing response, whereas the cationic Cd/Zn vacancies deteriorated sensor performance. Hydrogen and ethanol adsorption on ZnO(0001), ZnO(0001), and CdO(001) surfaces were studied theoretically using density functional theory to rationalize the experimental results. The oxygen ion-irradiated sensors exhibited better gas sensing responses than the argon ion-irradiated sensors for both analyte gases at an optimized operating temperature of 350 °C. Using combined experimental and theoretical evidence, we demonstrated the correlation between V_O concentration and gas sensitivity.

1. Introduction

The escalating levels of greenhouse gases and the phenomenon of global warming are major problems in the present decade. A substantial portion of these issues can be traced to the dependence on fossil fuels. Thus, the urgent need for the development of alternative renewable energy sources to replace fossil fuels has emerged [1]. In this regard, hydrogen (H₂) is identified as a viable candidate for generating clean and abundant energy. However, despite its benefits, H₂ is classified as hazardous due to its flammable and explosive characteristics [2], which raise safety concerns during its transportation and storage. This necessitates the advancement of high-performance hydrogen gas sensors, particularly for detecting fuel leaks in spacecrafts, automobiles, and aircraft, alongside a comprehensive assessment of their stability under

harsh radiation environments. Beyond its explosive characteristics, the ability to detect hydrogen at low concentration is essential to mitigate risks associated with oxidation in its pure oxygen-free form [3], and frostbite related to liquid cryogenic hydrogen, among others [4]. Therefore, ensuring rapid detection of hydrogen at low concentrations is essential for safety in industries with H₂-related components or byproducts. Furthermore, efficient H₂ sensing is also essential for aerospace applications, where NASA aims to transform aerospace power generation to enable new capabilities. Recent advancements in Proton Exchange Membrane (PEM) fuel cells, which use hydrogen and air as fuel and oxidant for ground transportation applications, have been noteworthy. NASA is also enhancing the performance of the space shuttle through the implementation of an alkaline fuel cell power system. In addition to alkaline fuel cells, researchers are exploring novel

E-mail address: arkaprava.das@umons.ac.be (A. Das).

^{*} Corresponding author.

fuel cells employing hydrogen peroxide, methane, and other sources. Consequently, for ground transportation, and particularly for space shuttles that utilize hydrogen in their fuel cells, verifying optimal fuel consumption will be of paramount importance. In addition to detecting H_2 , there is interest in detecting Volatile Organic Compounds (VOCs) in the atmosphere, which adversely affect air quality. The emission of VOCs from specific sources, including industrial wastewater, natural gas processing, petroleum refining, paints, and petrochemical processes, has emerged as a pressing environmental concern [5]. As a result, the detection of VOCs, such as acetone, ethanol, and methanol, at lower concentrations has become imperative due to their toxicity and highly flammable nature.

The synthesis of metal oxides and thin films, along with their functionalization, has generated great interest from researchers due to their robust applications [6]. Among various metal oxides, ZnO is a promising candidate for detecting both toxic and combustible gases [6]. ZnO-based nanostructures have demonstrated their potential as an efficient active layer for gas sensors to detect hazardous and toxic gases [7], including NH₃ [8], NO₂ [9], CH₄ [10], Acetone [11], CO [12], ethanol [12,13], and H₂ [10,14,15]. The need for sensitive and reliable electronic devices, such as gas sensors, to detect VOCs and flammable gases like H₂ at low concentrations in industrial settings is evident. ZnO nanostructured thin films, characterized by high sensitivity, low cost, and ease of synthesis, are promising candidates for active sensing layers in resistive gas sensors for electrical readouts. Contemporary ZnO-based gas sensors face three primary limitations that hinder their operational efficacy: slow response times, low target selectivity, and high operating temperatures. These challenges have traditionally been addressed through metallic ion doping strategies, as extensively documented in prior research [16]. Concurrent investigations have illustrated the effectiveness of alternative defect engineering methods, including electron/ion beam irradiation [17], gamma radiation exposure [18], or microwave treatment [19]. These irradiation techniques facilitate the controlled formation of defects within the semiconductor matrix, altering electronic state configurations by creating shallow and deep energy levels, thereby influencing the surface adsorption characteristics of target analytes. For instance, Ag⁷⁺ ion irradiation has been shown to enhance the sensitivity of ZnO sensors for methanol and ammonia [20]. Similarly, Xe ion irradiation has improved ZnO sensor performance for NO₂ detection [21]. The modifications induced by irradiation in the electronic, structural, and morphological properties also contribute to enhanced gas sensing performance [22].

A critical review of the current literature reveals significant methodological limitations within existing research paradigms. Predominant approaches artificially segregate doping and irradiation strategies, with current implementations restricted to cadmium concentrations below x≤ 0.20 in Cd_xZn_{1-x}O composite systems [5]. The existing findings regarding the irradiation-induced effects in the literature for ZnO-based sensors primarily focus on heavy ions, such as Ag and Xe, with energies in the hundreds of keV range. In contrast, this study employs irradiation with low kinetic energy (a few keV) and lighter ions, specifically O and Ar, at varying doses. Nanostructured Cd_xZn_{1-x}O (CZO) thin films with a high Cd concentration (x = 0.4) were irradiated with low kinetic energy ions to enhance the gas sensing performance. The detection of ethanol and H2 was demonstrated at different operating temperatures. The structural and morphological properties of pristine and irradiated thin films were studied with X-ray diffraction (XRD) and scanning electron microscopy (SEM) techniques. The electronic properties were investigated with X-ray absorption spectroscopy (XAS) and X-ray photoelectron spectroscopy (XPS). The influence of shallow energy electronic levels resulting from defects, particularly oxygen vacancies (VO), on gas sensitivity was examined. Furthermore, the adsorption of hydrogen and ethanol gases on the major wurtzite ZnO and rocksalt CdO surfaces, namely $ZnO(000\overline{1})$, ZnO(0001), and CdO(001), was computed using density functional theory (DFT). Table 1 summarizes the response values

Table 1
Response values for ZnO-based ethanol sensors at different operating temperatures.

Composition	Operating temp.	Ethanol concentration	Response (R _{air} /R _{gas})	Reference
$Cd_{x}Zn_{1-x}O (x = 0.10)$	350 °C	5 ppm	4	[23]
ZnO	400 °C	50 ppm	21	[24]
ZnO	250 °C	5 ppm	2.3	[25]
$Cd_xZn_{1-x}O (x = 0.10)$	300 °C	100 ppm	55 %	[26]
ZnO nanoparticles	350 °C	400 ppm	20.3	[27]
ZnO nanoparticles	350 °C	400 ppm	30.4	[28]
NiO/ZnO platelets	400 °C	100 ppm	12.0	[29]
CuO/ZnO nanowires	300 °C	100 ppm	28	[30]
Ag/ZnO nanoparticles	320 °C	100 ppm	12.1	[31]
Ag/ZnO nanoparticles	325 °C	50 ppm	32.5	[32]
Ag/ZnO nanorods	360 °C	100 ppm	36.5	[33]

for ZnO-based ethanol sensors, along with their operating temperatures.

1.1. Experimental methods

CZO thin films were deposited with a radio frequency (13.56 MHz) magnetron sputtering technique with a commercial Cd_xZn_{1-x}O ceramic target (40 wt % of Cd, purity 99.99 %) in Ar gas discharge. The pressure and power were fixed during the deposition at 0.007 Torr and 100 W, respectively. The distance between the substrate and the target was set at 10 cm. The deposition time was 20 min to achieve a thickness between 350 - 400 nm. The layer was deposited upon Pt interdigitated electrodes in alumina substrates. After the deposition, the sensors were irradiated with low-energy O and Ar ions at two different fluences. The samples were mounted on a copper block in the irradiation chamber. The irradiation was performed at a pressure of 10^{-6} Torr and at room temperature, with fluences of 1×10^{16} ions/cm2 and 5×10^{17} ions/cm². The beam energy was 3 keV, and the beam current was 50 µA during the irradiation. To achieve homogeneous irradiation throughout the active layer, the beam was scanned by an electromagnetic scanner with a surface area of 2×2 cm². Table 2 summarizes the details of the parameters used to irradiate the studied sensors.

X-ray diffraction (XRD) measurements were performed using the Bruker High-resolution X-Ray diffractometer system using Cu K_{α} beam in 20 range of 30° - 50°. Scanning Electron Microscopy (SEM) measurements were performed using a Hitachi TM-3000 model with an accelerating voltage of 15.0 keV. X-ray photoelectron spectroscopic (XPS) measurements were performed with Versa probe PHI 5000 from Physical Electronics, Chanhassen, MN, USA, using an Al K_{α} (1486.7 eV) beam. The XPS spectra were collected at a take-off angle of 45° with the electron energy analyzer, and the spot size was 200 μ m. The XPS spectra were fitted with a combination of Gaussian (70 %) and Lorentzian (30 %) functions, considering a Shirley background, using CASA software.

Table 2Ion irradiation parameters of the five sensors with composition Cd_{0.4}Zn_{0.6}O.

Sensor Acronym	Ion energy (keV)	Irradiating Ion	Irradiation fluence (ions/cm ²)
S1	0	pristine	0
S2	3	O_2	1×10^{16}
S3	3	O_2	5×10^{17}
S4	3	Ar	1×10^{16}
S5	3	Ar	$5 imes 10^{17}$

The binding energy calibration of the XPS spectra was done with the C 1s peak at 284.6 eV. Local electronic structure investigation using X-ray absorption near-edge spectroscopic (XANES) measurements has been performed for the Zn L_{3,2} and O K edges in surface-sensitive total electron yield mode at the PIRX beamline in the SOLARIS synchrotron, Poland [34,35]. XANES and XPS measurements were performed in an ultra-high vacuum chamber. For XANES data processing, we have used the standard script of the ATHENA software package (FEFF 6.0 code). The inflection point of the first derivative of the absorption spectra is considered the center of the leading absorption edge. When importing the raw data from the beamline, we perform background correction and normalize the data with the proper selection of pre- and post-edge ranges. Usually, we don't need to perform any significant background correction for oxide materials. For comparison purposes, we overlapped all data for the experiment to check whether the background was identical for all spectra. All our spectra are with the same background and have shown good reproducibility. We have selected 20 eV and 22 eV ranges in the pre-edge and post-edge regions, respectively, for both O K and Zn L_{3,2} edges, for normalizing the data. After normalization, the step difference in intensity along the Y-axis between the pre-edge and post-edge equals 1 [36].

The sensors were placed in a hermetically sealed Teflon chamber (35 cm³ of volume) during a typical gas sensing process. This chamber was connected to a gas mixing and delivery system. This system relied on accurately calibrated gas cylinders of pure dry air and the target gases. Initially, the surface of the samples was cleaned under a dry air flow for 5 h to stabilize their baseline resistance. Then, the samples were exposed to a given concentration of ethanol or H₂ diluted in pure air for 10 min, followed by a recovery cycle of 1 hour under dry air. To gauge the response of the sensors, the evolution of the resistance was continuously monitored using a high-precision multimeter (HP 34972A, Agilent). Hence, the sensing responses to both target gases were recorded at different operating temperatures, controlled by a Pt-heater screen printed on the sensor backside of the substrate. It is worth noting that the overall flow rate was kept homogeneous during all sensing tests. Specifically, mass-flow controllers and electro-valves were employed to adjust and maintain a steady flow of 100 mL/min.

1.2. Computational details

We have performed DFT calculations for hydrogen and ethanol adsorption on wurtzite ZnO and rocksalt CdO surfaces, specifically ZnO $(000\overline{1})$, ZnO(0001), and CdO(001). The first two are polar surfaces of the wurtzite structure, with O- and Zn-termination, respectively. These surfaces are usually present in crystallites and are considered the most important for surface reactions [37]. For CdO, we chose the {001} surface because, for ionic crystals in the rocksalt structure, it is the most stable and most abundant surface. The DFT calculations were performed using the projector-augmented-wavecode VASP [38]. We used the PBE exchange-correlation potential together with the DFT-D3 scheme for dispersion forces [39]. The plane-wave cut-off was set to 400 eV for CdO. For ZnO, we chose the larger value of 550 eV because polar surfaces might be numerically less stable. However, calculations with a lower cutoff of 400 eV gave almost the same results. The difference in adsorption energy between the two sets of cut-off energy was, at most, 0.03 eV. Adsorption was studied using 2×2 surface cells containing four cations and four anions, as well as slabs of 10 cation and 10 anion layers, resulting in a 3D supercell comprising 80 atoms in total. Repeated slabs were separated by at least 15 Å vacuum (see Fig. 9). For the k-space sampling, a $4 \times 4 \times 1$ Monkhorst-Pack mesh was used for CdO and a Gamma-centered $6 \times 6 \times 1$ mesh was used or ZnO. In the case of ZnO $(000\overline{1})$, the physical surface is O-terminated, and the opposite side of the slab is Zn-terminated. To saturate the dangling bonds of this non-physical surface, a layer of pseudo-hydrogen atoms with 1.5 electrons was added [40]. For the ZnO(0001) slab, pseudo hydrogen atoms with 0.5 electrons were added to saturate the dangling bonds of the lowest O layer. The atoms in the lowest three cation-anion layers, as well as the pseudo-atoms, were fixed at bulk positions. The positions of all other atoms were fully relaxed until the forces were lower than 0.01 eV/Å.

2. Results and discussion

2.1. Phase identification with XRD pattern

Fig. 1 shows the XRD patterns for S1, S3, and S5 sensors. Due to the high Cd concentration x = 40 %, the Bragg reflection for both wurtzite ZnO (JCPDS No. 36-1451) [41] and rocksalt CdO phase (JCPDS card No.36–1451) [42] is present in the XRD patterns. The reflections for the wurtzite phase (space group P6 3mc) are situated at 31.7° (100), 34.5° (002), 36.2° (101), and 47.6° (102). The peaks corresponding to the B1 and NaCl rock salt phase for CdO (space group Fm-3 m) are at 33.0° (111) and 38.4° (200), respectively. Therefore, hexagonal wurtzite and cubic rocksalt phases coexist in the XRD pattern. The samples irradiated with oxygen and argon ions at a kinetic energy of 3 keV exhibit no significant change in the XRD pattern: the lack of peak shift indicates the absence of tensile or compressive stress within the lattice. Typically, when the concentration of cadmium (Cd) is below the solubility limit, ionic substitution is anticipated. Conversely, when the Cd concentration exceeds the solubility limit, phase segregation occurs. A Cd concentration of 40 % surpasses the solubility limit, resulting in the observation of distinct CdO and ZnO phases in the X-ray diffraction (XRD) patterns. Nonetheless, this does not entirely rule out the possibility of ionic substitution, where Zn^{2+} ions (ionic radii $\sim 60 \text{ Å}$) may be replaced by Cd^{2+} (ionic radii \sim 70 Å). N. Gautam *et al.* have reported that a 5 % Cd concentration in ZnO does not exhibit a separate phase of CdO, whereas a 20 % Cd concentration leads to phase segregation between CdO and ZnO [43]. This observation aligns with the XRD patterns obtained for S1, S3, and S5 sensors.

By analyzing the full width at half maximum (FWHM) of the ZnO (100) peak and the CdO (111) peak, we have determined the nanocrystalline diameters for ZnO and CdO. The calculated diameters for ZnO are 29.5 nm, 29.5 nm, and 30.6 nm for the S1, S3, and S5 sensors. For CdO, the diameters are 31.9 nm, 34.5 nm, and 33.8 nm. The observed increase in the size of the CdO nanocrystallites is consistent with the understanding that CdO exhibits lower radiation hardness compared to ZnO.

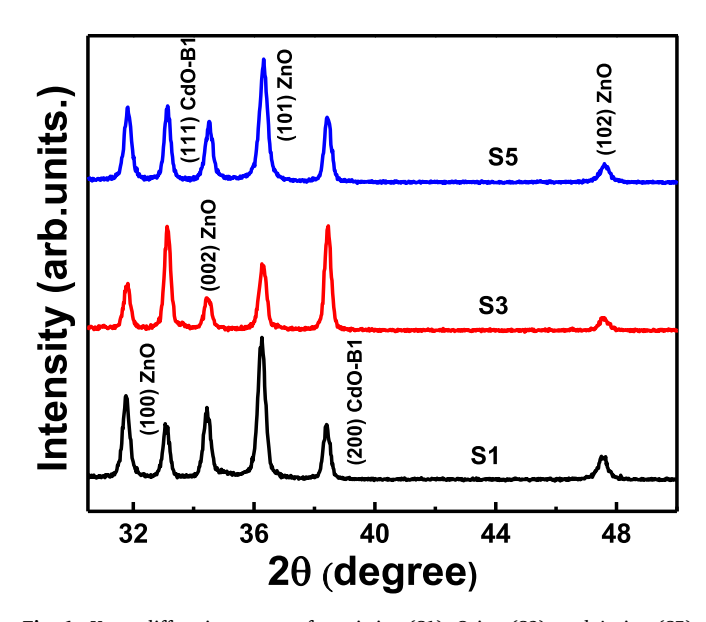


Fig. 1. X-ray diffraction pattern for pristine (S1), O ion (S3), and Ar ion (S5) ion irradiated $Cd_{0.4}O_{0.6}O$ thin films with fluence 5×10^{17} ions/cm².

2.2. Scanning electron microscopy

Fig. 2(a, b, and c) shows the SEM micrographs for S1, S3, and S5 sensors on a 1 μ m nm scale. The sensitive layers are homogeneous, and no cracks or dust particles are observed. Some void regions are present among the grains for all layers. Usually, ion irradiation induces grain growth. However, here, we have used low-energy ions, so significant grain growth is not expected. Therefore, oxygen and Ar ion irradiation have an insignificant impact on grain size. The grain size distribution directly impacts the diffusion of the analyte gas [44].

Fig. 2(a, b, c) illustrates the presence of pores in all sensor samples, namely S1, S2, and S3. Notably, the pores in S1 are characterized by a smaller size and a higher density, while the irradiated samples exhibit larger pores that are more sparsely distributed. From the gas sensing response, we have seen that irradiation with higher fluence has negatively impacted the sensing characteristics. The smaller nanograins are likely to exhibit a superior gas-sensing reaction [45]. The grain size-dependent sensing response can be explained by the migration of adsorbed gas molecules from the ambient atmosphere (oxygen gas molecules) at the surface of the grain boundaries. Those gas molecules, after adsorption, occupy the grain boundary area. Subsequently, it produces an electron depletion layer (EDL) at the interface between adjacent nanograins. This would lead to the formation of potential barriers, which subsequently hinder the flow of electrons across the grains. Therefore, this would enhance the resistance and reduce the number of electrons present in the conduction band. The gas sensing mechanism primarily relies on the principle of a change in the resistance of the EDL upon the introduction of analyte gas molecules. In most situations, the gas-sensing response is better for smaller grains [46]. Smaller grains with larger grain boundary areas can have more electrons trapped in the depletion layer. In the present scenario, no significant change in grain size is observed after irradiation. Therefore, a claim of substantial change in gas sensing response due to modification in grain size is not feasible.

Now, we will discuss the second aspect of morphology, i.e., porosity. For less porous and more compact thin films, theoretically, it is harder for analyte gas molecules to diffuse into the interior of the sensing materials. A more significant number of pores in $Cd_{0.4}Zn_{0.6}O$ thin films would provide more diffusion channels. The porous nature of the thin film provides more active sites for the generation of the electron depletion layer. Therefore, the presence of pores allows the formation of an electron depletion layer in both the outer and inner film surfaces [47]. In Fig. 2(c), we observe that thin films become more compact after Ar ion irradiation. Therefore, the observed reduction in sensing response (discussed in the upcoming section) after Ar ion irradiation is in good agreement with the observed morphological features of the thin films.

2.3. X-ray photoelectron spectroscopy analysis

XPS measurements are performed for all the sensors. Figs. 3(a, b) show the stacked survey scan and Cd 3d peak spectra for all five sensors. In the survey scan spectra in Fig. 3(a), the intense peaks correspond to

Cd 3d, Zn 2p, O 1 s, C1s, and Cd 3p peaks, which are situated at \sim 404.7 eV, 1020.3 eV, 532.4 eV, 284 eV, and 618.8 eV, respectively in the binding energy scale. Apart from these peaks, auger features are present in the survey scan spectra. Zn LMMb, Zn LMMa, Zn LMMc, O KLL, Cd MNN, and C auger peaks are situated at \sim 474.2 eV, 498.7 eV, 585.0 eV, 975.5 eV, 1110.4 eV, and 1221.8 eV in the binding energy scale. Apart from these, tiny peaks for Zn 2s, Zn 3s, Zn 3p, and Zn 3d are situated at 1195.0 eV, 136.5 eV, 87.8 eV, and 10.9 eV, respectively, in the binding energy scale. These values agree with previously reported survey scan spectra for ZnO and CdO thin films. Fig. 4(a, b) shows the stacked Zn 2p and O 1s peaks in XPS spectra for all the sensors. In Fig. 3(b), the Cd $3d_{3/2}$ $_2$ (411.3 eV) and $3d_{5/2}$ (404.5 eV) spin-orbit doublets are shown for all five sensors [48,49]. Apart from S1 and S2 sensors, an asymmetry feature in these peaks indicates the presence of Cd vacancies (V_{Cd}). Each peak of the doublet is fitted with two components corresponding to Cd-O and V_{Cd} [50]. Due to the generation of electron excitation-induced defects, the Cd 3d spectra shifted towards lower binding energies with irradiation. Such a shift towards lower binding energy with oxygen ion irradiation for Al-doped ZnO thin films was reported by Eui-Jung Yun et al. [51]. We have used the Voigt profile, which is a mixture of Gaussian (70 %) and Lorentzian (30 %) profiles. The Gaussian profile corresponds to finite experimental resolution, as well as various inhomogeneities, such as molecular packing and local morphology. The Lorentzian profile corresponds to a finite core hole lifetime [52]. Due to irradiation-induced shallow-level defects, the molecular packing, as well as the local morphology, is modified. The presence of defects alters core hole screening and core hole lifetime, thereby affecting the FWHM and contributing to the observed shift in binding energy for the core-level peak of a chemical element. This interplay provides a direct indication of surface functionalization resulting from ion irradiation. It is worth noting that changes in FWHM of the core level peaks can arise from surface charging effects. However, we can rule out this possibility as we used a conductive carbon tape between the film surface and substrate holder during the experiment. Furthermore, there are no other extrinsic sources that could account for changes in the FWHM of the core levels. In the present scenario, the observed change in FWHM is primarily attributed to surface modifications induced by irradiation. Consequently, we did not impose a constraint on the FWHM between pristine and irradiated thin films.

The area of the peak corresponding to V_{Cd} increased in the S3, S4, and S5 sensors. The amount of V_{Cd} is higher in Ar-ion-irradiated sensors due to higher nuclear energy loss, which causes the main reduction in sensitivity. Fig. 4(a) shows the Zn $2p_{3/2}$ core level centred at 1021.1 eV corresponding Zn– O bonding, i.e., the Zn²⁺ oxidation state in the ZnO matrix [53]. Analogously, Cd 3d and Zn 2p XPS spectra in Fig. 4(a) show a shift towards lower binding energy with O and Ar ion irradiation. The shift is prominent for S3, S4, and S5 sensors. The binding energy shift to a lower value suggests the formation of defects like Zn vacancies (V_{Zn}), oxygen vacancies (V_{O}), and oxygen interstitials (O_{i}) due to ion bombardment [51]. The presence of defects like V_{Zn} and V_{O} is well reported by Shin *et al.* for Xe ion irradiation on ZnO nanoparticles [21]. The Zn $2p_{3/2}$ spectra for S3, S4, and S5 sensors are fitted with two

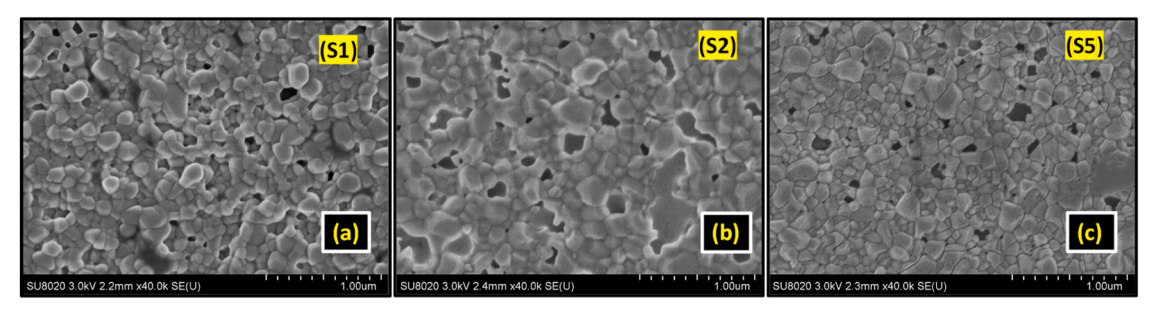


Fig. 2. SEM micrographs for pristine (a), O ion (b), and Ar ion (c) ion irradiated $Cd_{0.4}O_{0.6}O$ thin films with fluence 5×10^{17} ions/cm².

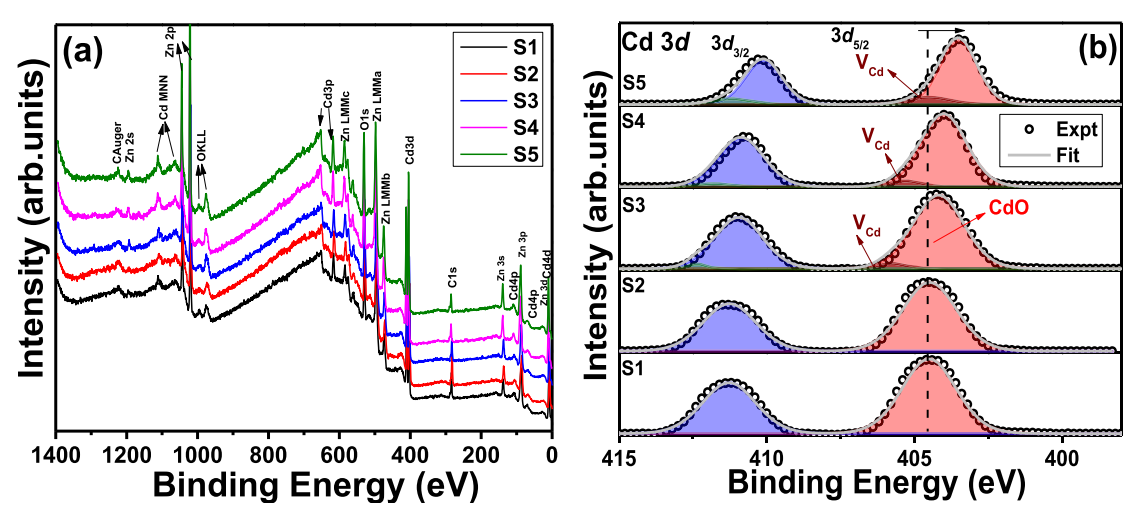


Fig. 3. (a, b): XPS survey scan spectra and Cd 3d peak spectra for all five pristine and irradiated sensors.

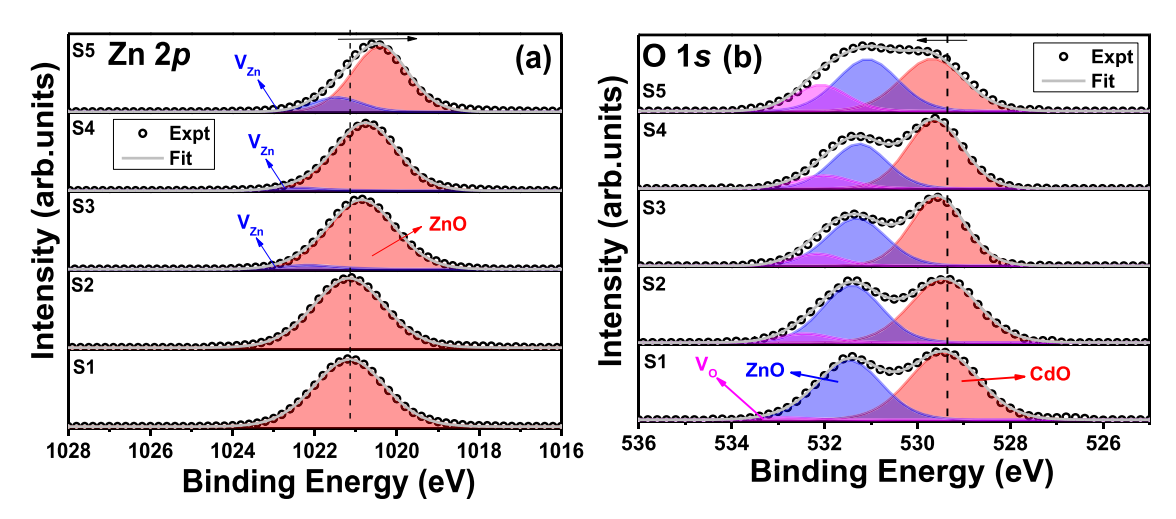


Fig. 4. (a, b): Zn 2p and O1s peaks XPS spectra for all five pristine and irradiated sensors.

components, Zn^{2+} and V_{Zn} . The area under the component corresponding to V_{Zn} increases for S3, S4, and S5 sensors, which is analogous to the V_{Cd} behaviour. Cationic vacancies in S3, S4, and S5 sensors lead to a deterioration in sensitivity, which is discussed in the upcoming section of the manuscript.

The O 1s core level spectra are shown in Fig. 4(b); for all the sensors, three components have been considered to deconvolute the O 1 s core level spectrum. The components centred at 529.4 eV, 531.4, and 533.0 eV correspond to Cd-O, Zn-O, and oxygen vacancies (V_O). The peak at 533.0 eV is attributed to O_r^- (O_2^- , and O_r^-) ions in the oxygen-deficient region owing to the presence of VO [54,55]. In the XRD pattern, separate phases of ZnO and CdO are present, which are compatible with deconvolution, considering Cd- O and Zn- O separately. The area under the Vo component increased with O and Ar ion irradiation, suggesting an increase in the number of Vo. Quantifying the formation energy of defects, such as cationic vacancies, cationic interstitials, and Vo, for this composite system requires a robust irradiation-based molecular dynamics simulation, which is beyond the scope of our present investigation. However, according to the literature, it is established that cation-related defects, including cationic interstitials, cationic vacancies, and Schottky-type defects, typically require a higher formation energy compared to Vo [21,56,57]. Therefore, Vo defects are observed in pristine S1 and oxygen-irradiated S2 sensors, where cationic vacancies are not observed. Shin et al. have reported that the possible formation of Schottky defects after ion irradiation results in the enhancement of $V_{\rm O}$ density in the irradiated sensors [21]. Therefore, the increasing intensity of the $V_{\rm O}$ component with ion irradiation indicates an enhanced density of $V_{\rm O}$ and reflects the possible presence of Schottky defects within the active sensing layer [21].

2.4. Soft X-ray absorption spectroscopy

2.4.1. Zn L_{3 2} edge

The normalized $Zn L_{3,2}$ XANES spectra for all sensors are shown in Fig. 5(a). The absorption edge starts from 1020 eV. The feature around 1023 eV marked with a1 is mainly contributed with Zn $2p \rightarrow Zn 4s$ transition. The designated a2 and a3 spectral features are primarily the result of Zn 2p to antibonding 3d state transitions [58]. There is also a contribution of 4s character unoccupancies in CB for the a3 feature. Due to the filled $3d^{10}$ orbital in ZnO, the pre-edge feature also contributes to a defect-induced local interference effect rather than transitions only coming from a bound state [59]. Theoretically, if one V_O is generated in the first coordination shell, a new feature in the pre-edge region is observed for the Zn K edge in ZnO. Furthermore, the intensity of this feature increases if a second $V_{\rm O}$ is considered in the second coordination shell [59]. Analogously, all the irradiated sensors, i.e., S2, S3, S4, and S5, present a feeble evolution in the a1 feature compared to the non-irradiated S1 sensor. This provides a direct indication regarding the presence of V_O around the photo-absorbing Zn atom. For better clarity,

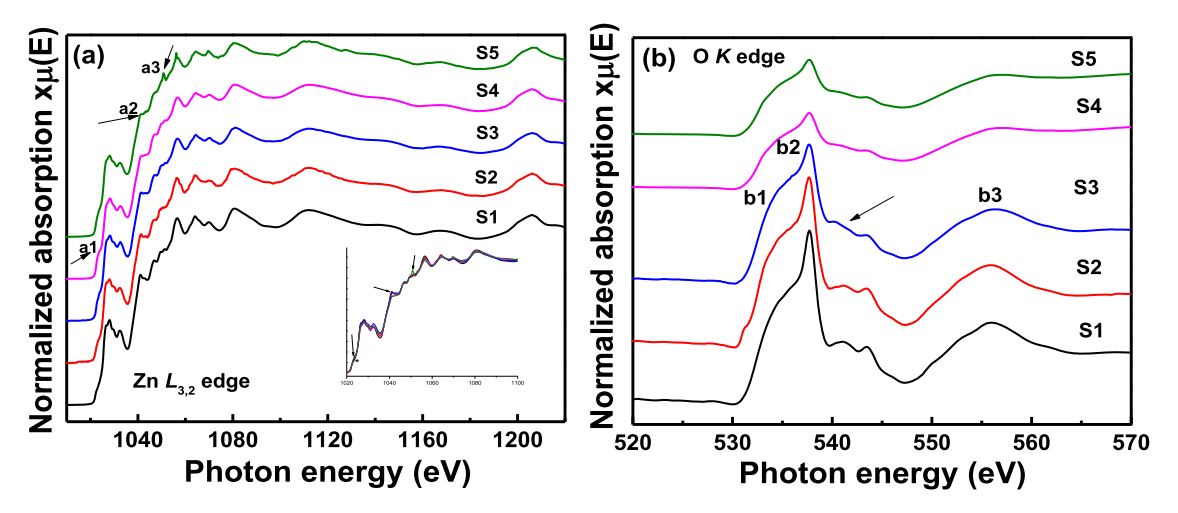


Fig. 5. (a, b): Normalized Zn $L_{3,2}$, and O K edges XANES spectra for pristine and irradiated sensors.

overlapped $Zn L_{3,2}$ spectra for all sensors are shown in the inset, where the feeble pre-edge evolution is indicated with an asterisk sign. The magnified inset Figure is provided in Fig. 1 of the electronic supplementary information (ESI) file for better visualization. There is hardly any variation in the S2, S3, and S4 sensors in the post-edge region compared to the S1 sensor. Due to irradiation, the possibility of the presence of V_{Zn} is less than V_O as the displacement energy for Zn and O is 65 eV and 42 eV, respectively [60]. If the presence of V_O affects the first coordination single scattering, its influence is also expected for a higher coordination shell. The random distribution of defects in the matrix is the reason for this observation. Earlier theoretical calculations of the Zn K edge for the Mn-doped ZnO system have indicated that XANES spectra cannot detect the impact of defects like Vo and Vzn with a random distribution inside the lattice [61]. V_{Zn} may be present for S3 and S4 sensors. However, due to the random distribution of these defects in the active sensing layer, $Zn L_{3,2}$ post-edge features don't indicate a significant change with O ion irradiation. There is an enhancement in intensity in the a3 feature for the S5 sensor and a reduction in the a2 feature for the S4 and S5 sensors. From this observation regarding the reduced intensity in the a2 feature, it is impossible to determine which point defects influence the intensity variation in the a2 and a3 features. Naturally, V_{Zn} may have reduced the density of antibonding 3d states, causing a reduction in the a2 feature. With higher concentrations of Vo in S5 sensors, the density of states for V_O is generated at the bottom of the CB, leading to a possible bound state transition from Zn 2p to those defect states [62]. This might have resulted in intensity enhancement in the a3 feature for the S5 sensor. There is also the possibility of electronic transitions from defects, such as Zinc interstitials in the irradiated sensors [63,64]. Electronic transitions from cationic interstitial defects to the density of states due to Vo can also be essential in changing a3 features.

2.4.2. O K edge

The normalized O K edges for all five sensors are stacked in Fig. 5(b). The region between 531 and 537 eV is associated with transitioning from O 1s to hybridized O 2p and Zn 4s orbitals. The region between b1 and b2 is the main absorption region. As the Zn 4s orbital is non-localized, the electronic transition from the O 1s core orbital to such a dispersive state produces a broad b1-like feature. Besides, the b2 feature is sharp and caused by a transition from O 1s to O $2p_z$ and $2p_{x+y}$ states. The transitions between 539 and 550 eV are attributed to the transition to hybridized O 2p and Zn 4p states, respectively. Beyond the b3 feature, the transition is mainly dominated by O 1 $s \rightarrow$ O2pZn4d states [65]. After irradiation, the b1 and b2 features don't show any significant change. In the region between b2 and b3, i.e., around 541.4 eV, a flat hump-like feature is absent for S3, S4, and S5 sensors. Therefore, the

irradiation-induced V_O might have reduced the hybridized antibonding O2pZn4p density of states, resulting in the absence of this feature in S3, S4, and S5 sensors. The overall intensity of the O K edge has been reduced for both S4 and S5 sensors. The lowering of overall spectral intensity with the presence of V_O has been theoretically reported by Demchenko et al. [66]. With Ar ion irradiation, the concentration of V_O is expected to be higher than in oxygen ion-irradiated sensors due to higher nuclear energy loss. This has been verified with XPS results. Therefore, the overall impact of V_O in lowering the spectral intensity is higher for S4 and S5 sensors.

2.5. Gas sensing analysis

The gas-sensing response for pristine and irradiated thin films has been investigated in the presence of hydrogen and ethanol gases at various temperatures. The response function indicates that the optimized temperature for the Cd_xZn_{1-x}O system to achieve an optimal response is 350 °C, which agrees with the existing literature [5,67,68]. Figs. 6(a) and 7(a) display the gas-sensing responses at various operating temperatures for H2 and ethanol, respectively. Before starting the experiment for both H₂ and ethanol, the sensors were kept at 350°C for 7–8 h under dry air to establish a stable baseline resistance. In Figs. 6(b) and 7(b), the real-time responses for the S1 sensor have been shown for H₂ and ethanol, respectively. The response function of a sensor is defined by the ratio R_a/R_g, where R_a and R_g are the resistances of the sensor in the reference gas (here, dry air) and the target gas, respectively. Interestingly, the S2 sensor indicates the best response at 350 °C in both gas exposures. The real-time resistance curves for the S1 sensor upon exposure to hydrogen and ethanol vapors at 350 °C are shown in Fig. 8 (a, b). The concentrations of H₂ and ethanol were fixed at 100 ppm (parts per million) and 10 ppm, respectively. The real-time responses for S3 and S4 sensors for hydrogen and ethanol gases, respectively, are shown in Figs. 2 and 3 of the ESI file. The overlapped real-time resistance curves for H₂ and ethanol analyte gases are shown in Fig. 4(a) and Fig. 4 (b), respectively, for S1, S2, S3, and S4 sensors.

2.5.1. H₂ gas sensing mechanism

The sensors have shown n-type behavior. Therefore, the gas sensing characteristics can be explained using the electron depletion layer (EDL) theory [69,70]. Once the $Cd_{0.4}Zn_{0.6}O$ sensor is exposed to air, the adsorption of O atoms on the film surface occurs. Electrons are extracted from the conduction band and transferred to the adsorbed O, further forming reactive oxygen species like O^2 , O_2 , O. The creation of reactive O species is expressed with the following chronological reactions.

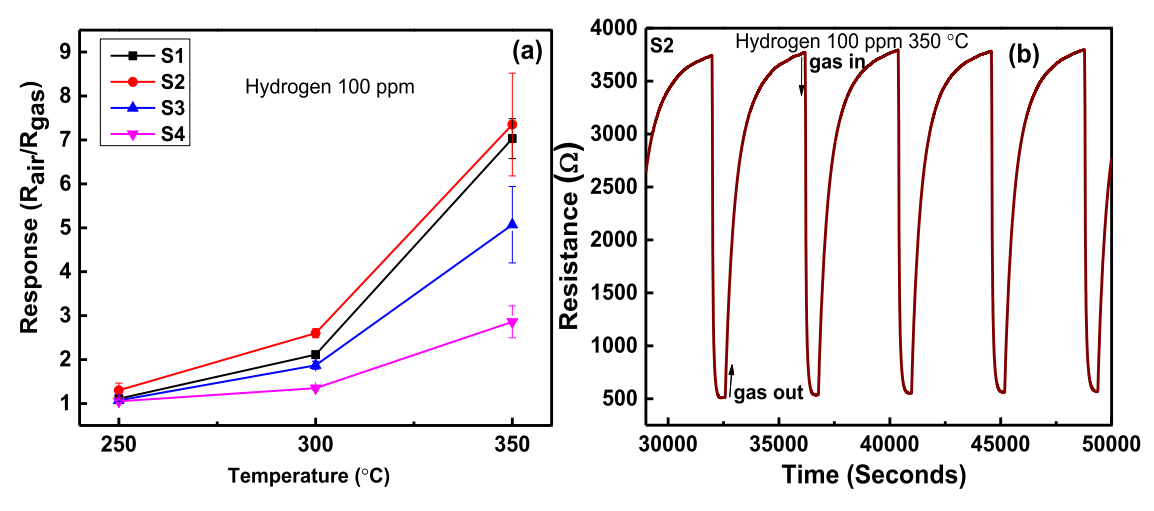


Fig. 6. (a) Response of S1, S2, S3, and S4 sensors with 100 ppm hydrogen gas analyte gas at three different operating temperatures; (b) Real-time resistance with 100 ppm hydrogen gas at 350 °C operating temperature for the S2 sensor.

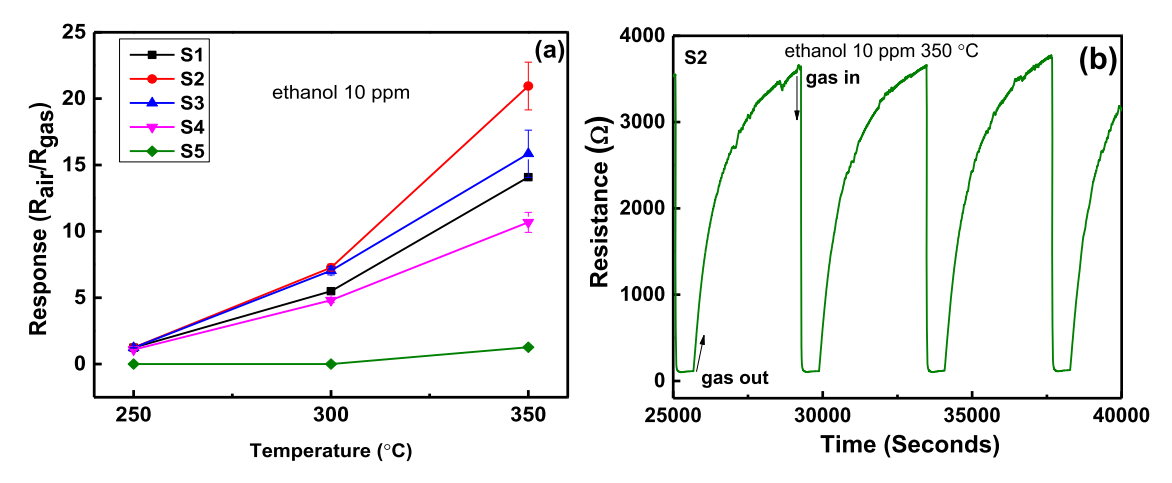


Fig. 7. (a) Response of S1, S2, S3, S4, and S5 sensors with 10 ppm ethanol gas analyte gas at three different operating temperatures; (b) Real-time resistance with 10 ppm ethanol gas at 350 °C operating temperature for the S2 sensor.

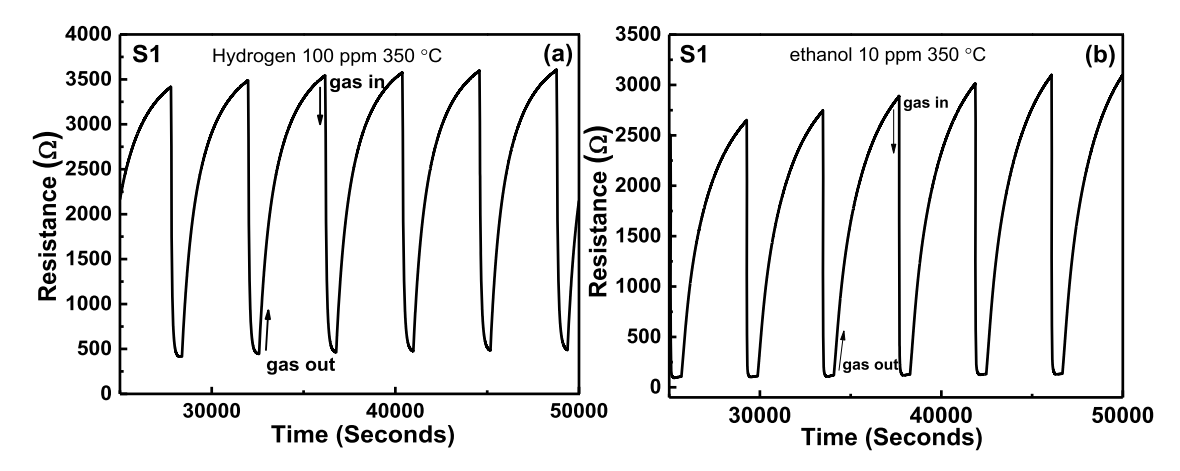


Fig. 8. Real-time resistance curves for oxygen irradiated (1 \times 10¹⁶ ions/cm² fluence) S1 sensor for hydrogen (a) and ethanol analyte (b) gases at 350 °C operating temperature.

$$O_{2\ (gas)} \rightarrow O_{2(adsorbed)}$$
 (1) $O_{2(adsorbed)}^{-} + e^{-} \rightarrow 2O_{(adsorbed)}^{-}$ (3)

$$O_{2(adsorbed)} + e^- \rightarrow O_{2(adsorbed)}^-$$
 (2) $O_{(adsorbed)}^- + e^- \rightarrow O_{(adsorbed)}^-$ (4)

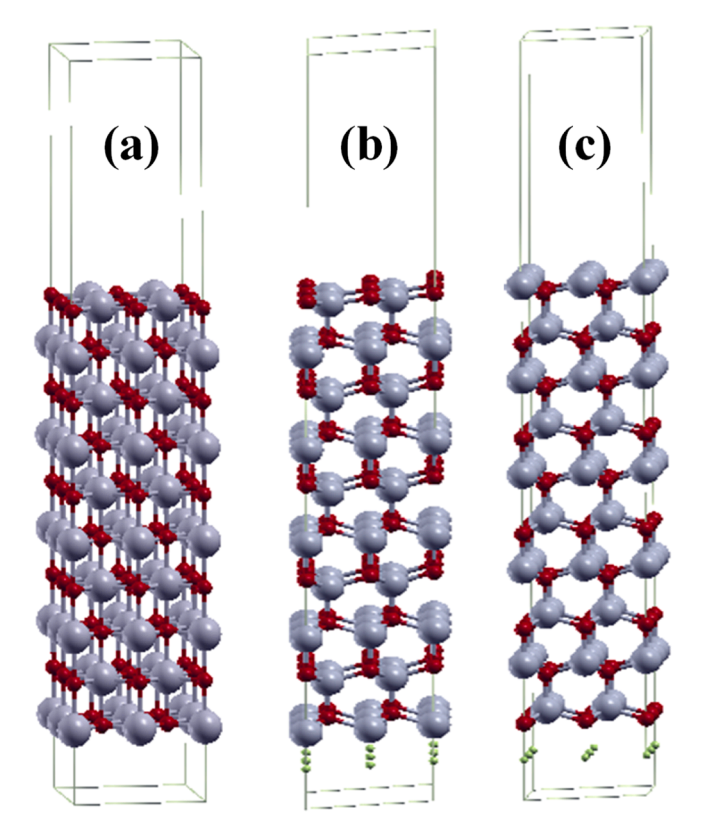


Fig. 9. Repeated slab structure with 80 atoms for adsorption energy calculation with 15 Å separation for rocksalt CdO(001) (a), wurtzite $\text{ZnO}(000\overline{1})$ (b), and ZnO(0001) (c) surfaces.

At 350 °C operating temperature, ${\rm O}^{2-}$ species are most likely to be formed. Consequently, the electrons in the reactions above generate a surface charge depletion layer. This depletion layer hinders the mobility of the electrons between adjacent grains and thereby enhances the sensor resistance [68,71]. Furthermore, the sensor resistance in air, i.e., Ra, becomes stable due to the saturation of oxygen adsorption at the surface. Here, the exposure of the target gas liberates the electrons trapped at the oxygen surface species, releasing them back to the CB.

Two pathways of adsorption processes are anticipated to take place for hydrogen sensing. First, the enhancement in conductance upon exposure to $\rm H_2$ can be attributed to the donor effect of protons. These electrons can be transferred to the CB, reducing resistance. The generation of protons with a fast reaction process is represented in the following reaction.

$$H_{2(gas)} \rightarrow H_{2(adsorption)} \rightarrow H_{(adsorption)} + H_{(adsorption)}$$
 (5)

$$H_{(adsorption)} \rightarrow H_{(adsorption)}^+ + e^-$$
 (6)

Another possible interaction route can be induced through a high-temperature (300 $^{\circ}\text{C}$) mediated interaction between maj H à la puissance plus and the O atom residing at the surface, creating surface hydroxyl groups. Now, these hydroxyl groups generate oxygen vacancies (V_O) via the creation of water [72]. These V_O inject electrons back into the CB and reduce the resistance. These reactions can be represented with the following steps.

$$2H^{+}_{(adsorption)} + 2e^{-} + 2O_{(surface\ site)} \rightarrow 2OH_{(adsorption)}$$
 (7)

$$2OH_{(adsorption)} \rightarrow H_2O_{(adsorption)} + O_{(surface\ site)} + V_O^{2+} + 2e^- \tag{8}$$

The withdrawal of $\rm H_2$ gas induces the desorption of the reaction products from the active layer. Further, the adsorption of oxygen molecules from the ambient at the surface, which subsequently fills the $\rm V_O$

electronic levels through the reaction [73,74]:

$$V_O^{2+} + \frac{1}{2}O_2 + 2e^- \leftrightarrow O_{0(surface \ site)}$$
 (9)

2.5.2. Ethanol sensing mechanism

The EDL creation is followed by reactions from (1) to (4). The formation of EDL at the surface would increase the resistance of the sensor. The adsorbed oxygen species react with the analyte gas molecule when ethanol vapor is introduced. The electrons generated from this reaction are transferred back to the CB of the sensor. This causes the thinning of the EDL and further reduces the resistance of the sensor [71]. These chemisorbed oxygen species impact the conductivity at the surface of the oxide semiconductor layer. The oxidation reaction of ethanol forms acetaldehyde and liberates electrons, H_2O . These electrons are reinjected into the CB, further reducing the resistance. The probable reaction mechanism is shown in the following chemical reactions.

$$CH_3CH_2OH_{(gas)} + O^- \rightarrow CH_3CHO + H_2O$$
 (10)

$$CH_3CH_2OH_{(gas)} \rightarrow C_2H_4 + H_2O \tag{11}$$

The reaction (10) indicates that acetaldehyde is expected to be formed, whereas reaction (11) initiates ethylene formation. However, the formation of acetaldehyde or ethylene depends upon the nature of the oxide surface layer. If the surface is acidic, ethylene formation takes place, and for the basic surface dehydrogenation process, i.e., acetal-dehyde is formed [75,76]. Finally, both will form CO_2 and H_2O . In summary, the formation of CO_2 and H_2O can be described by the following reaction equation:

$$CH_3CH_2OH_{(gas)} + 6O_{(adsorbed)}^- \rightarrow 2CO_{2(gas)} + 3H_2O + 6e^-$$
 (12)

$$CH_3CH_2OH_{(gas)} + 6O^2_{(adsorbed)} \rightarrow 2CO_{2(gas)} + 3H_2O + 12e^-$$
 (13)

For comparison purposes regarding the gas sensing response along with oxygen ion irradiation for H_2 (100 ppm) and ethanol (10 ppm), the response and recovery times are shown in Figs. 5(a, b) and 6(a, b) of ESI, respectively. The sensor is more sensitive toward ethanol than H_2 . The better sensitivity for ethanol was observed for pristine and irradiated sensors independently of the operating temperature. The higher sensitivity of ethanol is associated with higher chemical reactivity, resulting in a better response for the oxide sensing layer [77–79].

The oxygen ion irradiated sensors with $1\times 10^{16}~\text{ions/cm}^2$ fluence showed an improved sensitivity for ethanol. For hydrogen, the sensing response doesn't improve significantly with oxygen ion irradiation. To compare the sensitivity of the S2 sensor with pristine S1, Fig. 5(a, b) of ESI shows the sensitivity functions for S1 and S2 sensors for ethanol. Response time is defined as the time required to achieve 90 % of the maximum change in resistance upon exposure to the analyte gas. Recovery time is the time required to return to 90 % of the initial resistance, i.e., the resistance in the presence of dry air. Fig. 4(a, b) of ESI shows the response and recovery time for S1 and S2 sensors with H2. The recovery time (T_{off}) has reduced from 2347 s to 1706 s, and the response time (Ton) has reduced from 154 s to 147 s. In Fig. 5(a, b) of ESI, the response and recovery times have been calculated for S1 and S2 sensors in ethanol gas; with oxygen ion irradiation, both response and recovery times have indicated a decrement. The $T_{on}\,\mbox{has}$ reduced from 42 s to 28 s. Similarly, Toff has reduced from 2682 to 2437 s. No compressional or tensile strain is observed from the XRD pattern, and morphological features from SEM also don't show any significant change with oxygen or Ar ion irradiation. Therefore, the improved sensitivity can be correlated with irradiation-induced shallow energy levels generated by defects, such as Vo. Vo in ZnO/CdO has lower formation energy and is chemically active, generating donor levels in the band gap of the Cd_{0.4}Zn_{0.6}O system. The formation of V_O takes place via the following process [21]:

$$O_{-}O$$
 (surface site) $\rightarrow \frac{1}{2}O_{2(gas)} + V_{O}^{\bullet \bullet} + 2e^{-}$ (14)

 $V_0^{\bullet \bullet}$ indicates the oxygen vacancy with two effective positive charges. The electrons released are captured by the oxygen of the environment at the film surface. Oxygen ion irradiation induced Vo add electrons in the active layer which captures the oxygen and enhances the resistance of the active layer. The formation of Vo in the S2 sensor is supported by XPS observation in Fig. 4(b). V_O is present in S1 and S3 also. For S1, S2, and S3, the area under the deconvoluted V_O component is 2 %, 4 %, and 5 % of the O 1s peak, respectively. Therefore, the amount of V_O is even higher in the S3 sensor where O irradiation has been performed with 5 \times 10¹⁷ ions/cm² fluence. Even though the V_O is higher in S3 than in S2, the sensitivity is reduced in the S3 sensor as compared to the S2 sensor. At higher irradiation doses, Zn/Cd cation vacancies are probably generated, leading to the creation of holes. These holes effectively combine with the free electrons generated from V_0 [21]; thus, less oxygen from the air is adsorbed. The presence of cation vacancies is supported by XPS Zn 2p and Cd 3d XPS spectra in Figs. 3(b) and 4(a), where both Cd and Zn vacancies are observed for S3, S4, and S5 sensors. For Ar ion irradiation, the sensitivity was reduced in S4 and S5 compared to S1. Therefore, in this material, the 3 keV Ar ion irradiation is not suitable to improve sensor performance. The nuclear energy loss with 3 keV Ar ion in ZnO and CdO matrix are 68.7 eV/Å and 61 eV/Å, respectively. The same with 3 keV O ion in ZnO and CdO matrix are 2.56 eV/Å and 2.19 eV/Å (The energy values are calculated from SRIM 2013 code). Therefore, the probability of creating shallow-level defects in the surface is relatively higher with Ar ion irradiation, as the energy deposition via elastic collision with the atoms is more than double compared to O ions. Apart from V_O, the point defects, such as Zn/Cd cation vacancies, are also increased with Ar irradiation, resulting in a reduction in sensitivity. For S5 only, when operated at 350 °C showed a feeble response to ethanol vapour. Apart from that, the S5 sensor doesn't show any response to other gases at any operating temperature. From energy-dispersive X-ray spectroscopy (EDX) measurements, we have determined the elemental distribution of Cd, Zn, and O before and after irradiation with a fluence of 5 \times 10^17 ions/cm². The EDX measurements for three thin films, along with their weights and atomic percentages for Cd, Zn, and O, are provided in the ESI at Figs. 6, 7, and 8. The atomic and weight percentage values are provided in Tables 1, 2, and 3. With Ar ion irradiation, possibly a few of the Cd atoms are sputtered out of the surface region, which reduces the atomic and weight percentage of the thin film. The sputtered Cd atoms will create vacancies, which have deteriorated the gas sensitivity for the S5 sensor. This is due to Ar ion irradiation with higher fluence, causing significant damage to the surface.

The resistance transient for pristine and irradiated sensors was measured at three different operating temperatures. Apart from ZnO-based sensors, these phenomena have also been observed in other semiconductor metal oxides [67]. The reducing gas molecules may not acquire sufficient energy to activate the interaction with adsorbed O species. However, at higher temperatures, the required activation energy is readily obtained, triggering and accelerating the reaction between the reducing gas and the adsorbed O species. Therefore, the concept of activation energy explains the concurring enhancement of

Table 3Calculated adsorption energy values for all structures with consideration of defects. The number in parentheses indicates the adsorption energy for the same system, but with an oxygen vacancy in the bulk.

E _{ads} (eV)	Н	C ₂ H ₅ OH	$C_2H_5O + H$
CdO(001)	1.103	0.853	
$CdO(001)-V_O$	0.509	0.828	1.479
$ZnO(000\overline{1})$	2.283	0.554	
$ZnO(000\overline{1})-V_O$	0.742 (0.738)	1.310	2.777
ZnO(0001)	0.547	0.882	
ZnO(0001)-V _{Zn}	0.942 (0.934)	0.895 (0.866)	

the response with increasing operating temperature. The adsorbed oxygen species and the active sites at the semiconductor surface are deficient at lower temperatures. It may lead to an incomplete reaction, resulting in a feeble response for the target gas at a lower temperature. With an enhanced operating temperature, the surface adsorption of oxygen species increases rapidly, leading to the generation of a thick depletion layer at the surface. When reducing gas is introduced, the change in transient resistance becomes more prominent. Beyond the optimum temperature, the desorption rate of the adsorbed oxygen species from the surface increases rapidly, resulting in a deterioration in the response. With further increments in temperature, enhancement of charge-carrier concentration and electrical conductivity, along with the reduction in Debye length, cause deterioration in the response [71]. In the present work, we kept the measurements limited to 350 °C, a reported optimum temperature for $Cd_xZn_{1-x}O$ based sensors.

The room temperature band gap and electron concentration and carrier mobility of CdO are ~ 2.18 eV, $\sim 10^{19}/\text{cc}$, and ~ 531 cm²/V.s, respectively. The room temperature band gap and electron concentration, and carrier mobility of ZnO are ~ 3.4 eV, $\sim 10^{17}$ /cc, and ~ 180 cm²/ V.s, respectively. When Cd impurity is incorporated in the ZnO host matrix, the band gap reduces. With Cd impurity, the electron concentration also increases, making the extraction process of electrons from the conduction band and their transfer to the adsorbed oxygen at the surface easier compared to ZnO thin films. The transfer of the electrons from the conduction band to the adsorbed O further forms reactive oxygen species and a subsequent surface charge depletion layer. Now, the exposure of the target gas liberates the electrons trapped at oxygen surface species, releasing them back to the CB. With Cd impurity better sensing response is expected as the charge depletion layer at the surface will be formed quickly at air exposure. The effective band gap of our binary oxide system is 2.82 eV, which is less than the band gap of ZnO. Therefore, the presence of CdO effectively lowers the conduction band minima and supports the formation of a surface charge depletion layer. When we see the sensor performance, it is the combined effect of both ZnO and CdO as nanocrystallites of both the oxides are present in the grains at the surface.

According to previous results, the amount of oxygen vacancies in a metal oxide semiconductor correlate well with the amount of surface hydroxyls found after exposing its surface to ambient moisture [80]. However, the promotion of oxygen vacancies has been found to enhance the gas sensing properties of metal oxides, even under humid conditions [81]. Therefore, we can anticipate that the presence of ambient moisture will have a detrimental effect on gas sensitivity; however, the benefits brought about by the generation of oxygen vacancies in samples that have undergone plasma treatment will still be evident. In addition, we expect moisture effects to be mild, considering the high operating temperature of 350 °C that will promote water desorption from the sensor surface [82].

2.6. DFT analysis and adsorption energy calculations

In order to shed light on the microscopic phenomenon responsible for the sensing, we studied the adsorption of hydrogen and ethanol on the most important CdO and ZnO surfaces, namely Cd(001), Zn(000 $\overline{1}$), and Zn(0001). We considered the pristine, defect-free surfaces and surfaces with O or Zn vacancies in the top-most surface layers. This gave the following six surface models: CdO(001), Cd(001)-V_O, ZnO(000 $\overline{1}$), ZnO(000 $\overline{1}$)-V_O, ZnO(0001), and ZnO(0001)-V_{Zn}, where -V_O and -V_{Zn} denote, respectively, an oxygen and a zinc vacancy in the surface layer. In the case of hydrogen adsorption, we assume dissociation of the H₂ gas molecule. While physisorbed H₂ molecules are likely to be also present in the samples, their effect on the resistivity can safely be neglected, because of the weak interaction of physisorbed hydrogen [83]. Our DFT calculations show that physisorbed H₂ may exist on these surfaces. The calculated adsorption energy per H₂ molecule is in the range of 0.1–0.2

eV, specifically 0.16 eV, 0.13 eV, and 0.17 eV for ZnO(000–1), ZnO (0001), and Cd(001), respectively. However, these physisorbed states are much less stable than dissociated, chemisorbed hydrogen, where the adsorption energy is between 1 and 4 eV per $\rm H_2$ (see Table 3 below). As a consequence, at sufficiently elevated temperatures, physisorbed hydrogen is unstable; the molecules will desorb or dissociate and chemisorb. Therefore, we focus on chemisorbed hydrogen in the rest of the paper. We consider the adsorption of one H atom per 2 \times 2 surface cell, i.e., the reaction:

$$\frac{1}{2} H_{2(gas)} \rightarrow H_{(ads)} \tag{15}$$

Both atoms of a hydrogen molecule might adsorb at the same oxygen surface atom. We checked this possibility for the defect-free $ZnO(000\overline{1})$ -O surface and found that the adsorption energy per H_2 molecule is 2.63 eV, less than the competing process of formation of two nearest neighbor hydroxyl groups with an adsorption energy per H_2 molecule of 4.30 eV. In other words, the reaction (8) is endothermic at the $ZnO(000\overline{1})$ -O surface.

For all other surfaces, we have limited ourselves to the adsorption of a single H atom according to Eq. (15). For ethanol, we consider the normal adsorption reaction:

$$C_2H_5OH_{(gas)} \rightarrow C_2H_5OH_{(ads)} \tag{16}$$

as well as the dissociative adsorption

$$C_2H_5OH_{(gas)} \to C_2H_5O_{(ads)} + H_{(ads)}$$
 (17)

We define the adsorption energy of a specie *X* as

$$E_{(ads)}(X) = -E(X/S) + E(S) + E(X)$$
(18)

where E(X/S) is the energy of X adsorbed on the surface, E(S) is the energy of the clean surface and E(X) is the energy of X in the gas phase.

In this definition, $E_{ads}>0$ means that the adsorption reaction is exothermic and that the adsorbed species is stable. Note that for X=H, we take $E(X)=\frac{1}{2}E(H_{2(gas)})$ according to Eq. (15). The calculated adsorption energies are listed in Table 3. The optimized adsorption structures, along with the adsorbed analyte gases, are shown in Fig. 10 (H adsorption) and Fig. 11 (ethanol adsorption).

Hydrogen adsorption: E_{ads} is in the range of 0.5 to 1.1 eV except on $ZnO(000\overline{1})$ where E_{ads} is considerably larger with 2.3 eV. It should be noted that the defect-free $ZnO(000\overline{1})$ surface has a surplus of holes. The formation of holes follows the reaction: $O_O^{\times} \rightarrow O'' + 2$ e^{\blacksquare} i.e., it is a p-doped system. The adsorption of $(H \rightarrow H^{\blacksquare} + e')$ electron reduces the p-doping. Here O'' is a di-negative oxygen ion and e' is the negatively charged electrons. O_O^{\times} is the neutral oxygen atom at the normal lattice oxygen site. e^{\blacksquare} denotes a hole. H^{\blacksquare} is a positively charged hydrogen ion. The notations for hole formation reaction are provided as proposed by Kroger and Vink [84].

The large adsorption energy shows that this strongly stabilizes the system. For the $\text{ZnO}(000\overline{1})\text{-}V_0$ surface, the H adsorption energy is much smaller (0.7 eV). The $\text{ZnO}(000\overline{1})\text{-}V_0$ model with 0.25 monolayer vacancy concentration used here exactly compensates the polarity of the $\text{ZnO}(000\overline{1})\text{-}V_0$ surface [25]. This stabilizes the surfaces, which recover the semi-conducting electronic state of undoped bulk ZnO, as we have checked.

As we have mentioned, in Eq. (5), the H_2 molecule can dissociate in the equilibrium condition with $(000\overline{1})$ -O surface for ZnO [37]. Subsequently, the hydrogen atom may get adsorbed and form an OH-group with the surface oxygen ions, as in Fig. 10 and Eq. (7). Now, the presence of V_0 is favorable up to the threshold concentration for ZnO $(000\overline{1})$ -O surface as it helps in charge compensation in an oxygen-rich environment. This subsequently helps in the better filling of the O 2p band. It has been reported theoretically by Mayer $et\ al.$ that for an 8 Zn-O double-layer thick slab, V_0 concentration up to $\frac{1}{4}$ endorses a partially

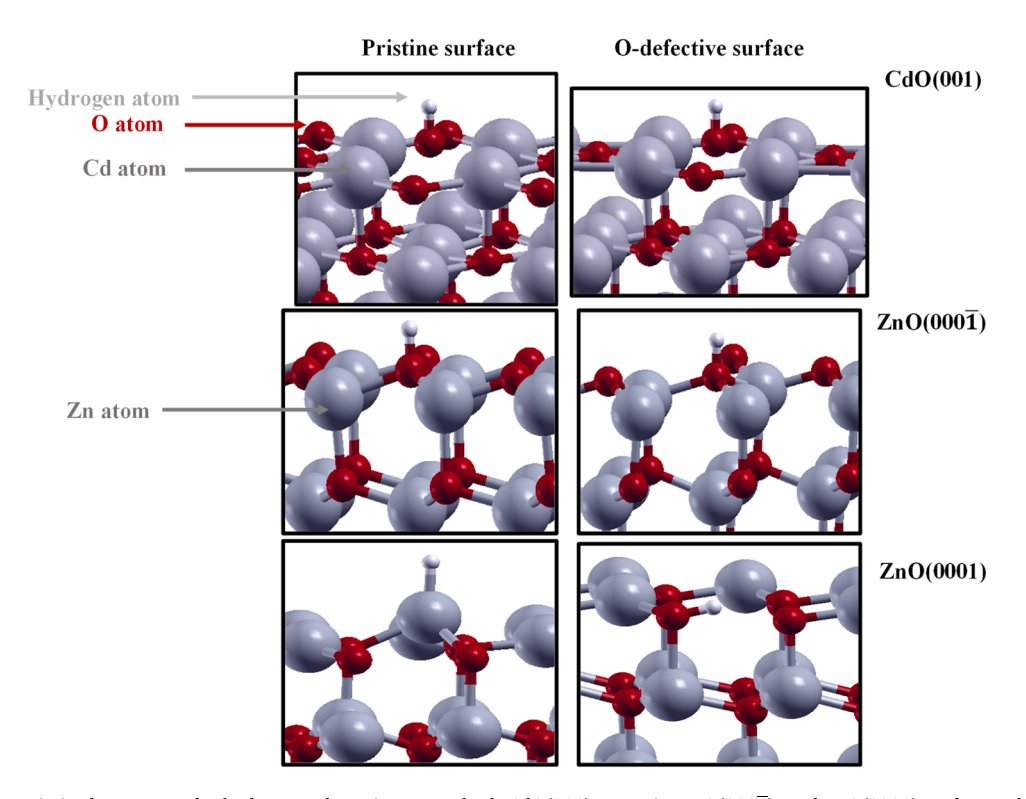


Fig. 10. Theoretically optimized structures for hydrogen adsorption on rocksalt CdO(001), wurtzite $ZnO(000\overline{1})$, and ZnO(0001) surfaces. The left column shows adsorption on pristine (i.e., defect-free) surfaces, and the right column shows adsorption on surfaces with one oxygen vacancy. Hydrogen, oxygen, and metal atoms (Zn or Cd) are represented as small white, medium red, and large grey spheres, respectively. For the ball radii, we chose elemental default values that roughly scale with the neutral atomic radii rather than the divalent ionic radii. The latter are $O^{2-}\sim1.27$ Å, $Cd^{2+}\sim0.97$ Å, and $Cd^{2+}\sim0.74$ Å.

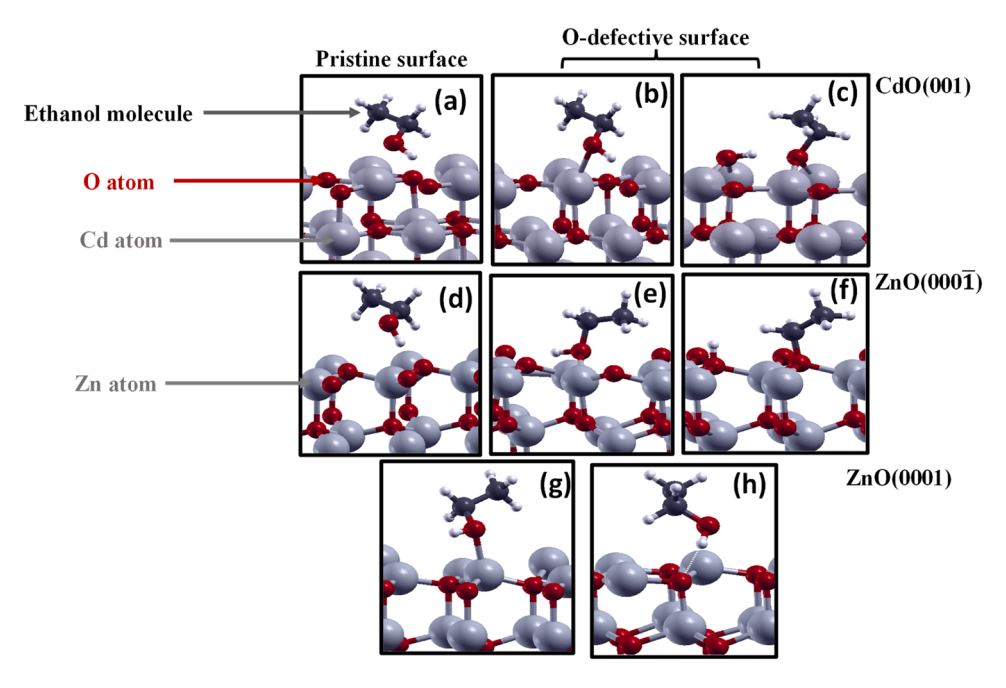


Fig. 11. The optimized structures for ethanol adsorption for rocksalt CdO(001), wurtzite $ZnO(000\overline{1})$, and ZnO(0001) surfaces. Hydrogen, oxygen, and metal atoms (Zn or Cd) are represented as small white, medium red, and large grey spheres, respectively. Figure (a), (d), and (g): pristine surface; (b) and (e): O-defective surface without ethanol dissociation; (c) and (f) O-defective surface with ethanol dissociation; (h) Zn-defective surface.

occupied O 2p band, which is crucial for stabilizing the $(000\overline{1})$ -O surface [37]. Beyond that concentration, the O 2p band is occupied, and further filling of the Zn-4s-like valence band, i.e., surface n-doping, would commence. This, in turn, leads to a higher energy cost for removing oxygen from the surface. However, the combination of V_O and H adatom in the $ZnO(000\overline{1})$ -O surface, which is the present case of concern, is not reported to be thermodynamically stable [37]. For stabilizing the ZnO (0001)-O surface in ZnO, an extremely low concentration of hydrogen with an oxygen-rich atmosphere is required, which is not possible experimentally [37]. In our experimental scenario, the response and recovery time improved with low kinetic energy O ion irradiation. So, shallow-level defects like V_O due to irradiation and a combination of hydrogen adatom improved the response and recovery time. Yan et al. reported that the majority of the charge density of the defect state is localized around V_0 [85]. Therefore, it is quite possible that when an H_2 molecule is adsorbed, a spontaneous charge transfer of two electrons takes place, filling the antibonding σ_{1s}^* molecular hydrogen orbital. This filling would subsequently facilitate the dissociation of H2 molecules in hydrogen atoms and may trigger easier H adsorption. Similar facilitation of O2 molecule dissociation in the presence of V0 is theoretically reported for the ZnO $(10\overline{1}0)$ surface by Yan et al. [85].

For CdO, the situation is straightforward to understand. It is a wellestablished fact that CdO is a non-stoichiometric metal oxide with a large number of free electrons due to V_O defects [86]. So, most carriers in CdO are electrons, which participate in the electrical conduction phenomenon. One Vo in the bulk can generate six five-fold coordinated Cd atoms [87]. Therefore, after O ion irradiation, we can expect the presence of such virtually unsaturated Cd atoms due to Vo generation, which can be considered a source of free electrons. These Cd atoms in the CdO lattice can adsorb O₂ molecules from the ambient due to V_O. The adsorbed oxygen molecules capture the available free electrons from the CdO lattice and further form O_2^- and O^- ions [88,89]. This further results in the formation of a depletion layer where the amount of conduction electrons is minimal. When the surface is exposed to H2, the trapped conduction electrons in the depletion layer are released, leading to a change in electrical conductivity upon H2 exposure. Therefore, a greater number of Vo defects facilitates the adsorption of more O2

molecules from the ambient by unsaturated Cd atoms, causing a high resistance value at the surface. With a higher concentration of V_O, more O_2^- and O_2^- ions can be converted into water vapour in the presence of H_2 molecules. This suggests that the adsorption of H2 molecules in CdO is enhanced in the presence of V_O defects. As a result, the response function improves with oxygen ion irradiation. In our composite $Cd_xZn_{1-x}O$ (x =0.4) thin films system, ion irradiation may have induced the formation of Vo in both ZnO and CdO lattices. Theoretically, the adsorption energy is reduced for both the $ZnO(000\overline{1})$ - V_O and CdO(001)- V_O surfaces, which may seem at odds with an overall enhancement in the response function for hydrogen gas sensing in Fig. 6(a) for the S2 sensor. However, it should be noted that the experiments are conducted in ambient conditions with a high partial pressure of oxygen. We have checked by DFT calculations, that O2 molecules preferentially adsorb at V0 to form ZnO $(000\overline{1})$ - V_0+O_2 or CdO(001)- V_0+O_2 with an adsorption energy per O_2 molecule of 1.18 eV or 2.12 eV, respectively. When hydrogen is adsorbed at $ZnO(000\overline{1})-V_O+O_2$, the H adsorption energy is 2.10 eV, which is close to the value of the pristine $ZnO(000\overline{1})$ surface (2.28 eV). In the case of CdO(001)-V_O+O₂, the H adsorption energy is 1.03 eV, again very close to that of the pristine CdO(001) surface (1.10 eV). So, when the oxygen vacancies (V_O) are filled with O₂, the H adsorption energies are almost the same as for the pristine surfaces.

Ethanol adsorption: When the ethanol molecule doesn't dissociate, E_{ads} is in the range of 0.5 to 1.3 eV. We found that ethanol can dissociate at a V_O according to reaction (16) both on CdO(001)- V_O and ZnO(000 $\overline{1}$)- V_O . The O-atom of the ethanol molecule fills the V_O , and the H atom adsorbs on a neighboring O surface site, as shown in Fig. 11 (e and f). For such dissociative adsorption, the adsorption energy is larger by 0.65 eV (CdO) or 1.45 eV (ZnO) than for non-dissociative adsorption. As seen from Table 3, dissociative adsorption of ethanol at the O-defective surfaces has a larger adsorption energy than (non-dissociative) adsorption on the pristine surfaces, indicating that the presence of V_O tends to enhance the ethanol sensing response in agreement with the experimental findings for samples S2 and S3 in Fig. 7.

We also studied the effect of V_0 in bulk in a few cases. To this end, we created an oxygen vacancy in the center of the slab, i.e., five layers below the surface. The corresponding adsorption energies are given in

parenthesis in Table 3. Bulk $V_{\rm O}$ only has a small effect on the adsorption energy. The adsorption energy is slightly reduced in absolute value, but the difference is below 0.03 eV in all cases.

3. Conclusion

We studied the impact of low kinetic energy oxygen and argon ion irradiation on hydrogen and ethanol gas sensing characteristics of Cd_{0.4}Zn_{0.6}O nanostructured thin film. Structural and morphological properties were investigated with XRD and SEM techniques. However, no notable modification was found with irradiation. XPS and XAS indicated an increase in the number of oxygen vacancies with increasing fluence of irradiation. At 350 $^{\circ}\text{C}$ operating temperature, with 1 \times $10^{1\overline{6}}$ ions/cm² fluence for O ion irradiation, sensor S2 has shown a marginal improvement in gas sensing response for both analyte gases. However, further increments in fluence degraded the sensor performance due to the creation of holes resulting from ZnCd cationic vacancies. Furthermore, due to higher nuclear energy loss, Ar ion irradiation has degraded the gas sensitivity even with lower fluence. To optimize the sensitivity of a sensor, parameters like the ion kinetic energy and fluence need to be adjusted so that the number of electrons forming EDL and surfaceadsorbed oxygen species is maximized. In sensor S2, the number of V_0 , which are the preferential adsorption sites, is higher with 1×10^{16} ions/cm² fluence of oxygen ion irradiation compared to the other sensors. The adsorption energy values calculated from DFT for hydrogen gas decreased when V_O at $ZnO(000\overline{1})$ - V_O and CdO(001)- V_O surfaces as considered. Through defect engineering using ion irradiation, the performance of other metal oxide-based sensors of a similar nature can be enhanced. The integration of doping and low kinetic energy irradiation to customize material properties for diverse applications, such as gas sensing and resistive memory switching devices, represents a promising technique for optimal efficiency.

Data availability statement

All data are included in the manuscript and supplementary file. However, we agree to share any specific information and data files upon request for readers.

CRediT authorship contribution statement

Arkaprava Das: Writing – review & editing, Writing – original draft, Visualization, Validation, Project administration, Methodology, Investigation, Funding acquisition, Formal analysis, Data curation, Conceptualization. Peter Krüger: Writing – review & editing, Visualization, Software, Methodology, Investigation. Shuja Bashir Malik: Writing – review & editing, Methodology. Juan Casanova-Chafer: Writing – review & editing, Methodology. Fatima Ezahra Annanouch: Methodology. Ewa Partyka-Jankowska: Methodology. Marcin Zając: Methodology. Eduard Llobet: Writing – review & editing, Methodology. Carla Bittencourt: Writing – review & editing, Validation, Supervision, Methodology.

Declaration of competing interest

The authors declare that they have no known competing financial interests or personal relationships that could have appeared to influence the work reported in this paper.

Acknowledgements

This publication was partially developed under the provision of the Polish Ministry and Higher Education project "Support for research and development with the use of research infrastructure of the National Synchrotron Radiation Centre SOLARIS" under contract nr 1/SOL/

2021/2. We acknowledge SOLARIS Centre for the access to the PIRX beamline, where the measurements were performed. We would like to thank Dr. Adriano Panepinto, Dr. Xavier Noirfalise, and Dr. Axel Hemberg for their assistance. A. Das acknowledges Wallonie Bruxelles International post-doctoral funding for providing scholarship during this research work. A. Das is thankful to FNRS for providing a mobility grant to perform the XAS measurements at PIRX, Solaris. J.C.-C. is supported by the Marie Skłodowska-Curie grant agreement No. 101066282—GREBOS. E. Llobet is supported by the Catalan Institution for Research and Advanced Studies (ICREA) via the 2023 Ed. of the ICREA Academia Award. CB is a research associate of FNRS-Belgium.

Supplementary materials

Supplementary material associated with this article can be found, in the online version, at doi:10.1016/j.surfin.2025.107862.

Data availability

All data are included in the manuscript for the readers.

References

- [1] S. Agarwal, S. Kumar, H. Agrawal, M.G. Moinuddin, M. Kumar, S.K. Sharma, K. Awasthi, An efficient hydrogen gas sensor based on hierarchical Ag/ZnO hollow microstructures, Sens. Actuators. B Chem. 346 (2021) 130510.
- [2] A. Katoch, S.-W. Choi, H.W. Kim, S.S. Kim, Highly sensitive and selective H2 sensing by ZnO nanofibers and the underlying sensing mechanism, J. Hazard. Mater. 286 (2015) 229–235.
- [3] W.J. Brown, National aeronautics and space administration, (1997).
- [4] S. Chatterjee, E. Shkondin, O. Takayama, A. Fisher, A. Fraiwan, U.A. Gurkan, A. V. Lavrinenko, G. Strangi, Hydrogen gas sensing using aluminum doped ZnO metasurfaces, Nanoscale Adv. 2 (2020) 3452–3459.
- [5] S.P. Bharath, K.V. Bangera, G.K. Shivakumar, Properties of CdxZn1-xO thin films and their enhanced gas sensing performance, J. Alloys. Compd. 720 (2017) 39–46.
- [6] S. Bai, S. Chen, Y. Zhao, T. Guo, R. Luo, D. Li, A. Chen, Gas sensing properties of Cd-doped ZnO nanofibers synthesized by the electrospinning method, J. Mater. Chem. Mater. 2 (2014) 16697–16706.
- [7] V.S. Bhati, M. Hojamberdiev, M. Kumar, Enhanced sensing performance of ZnO nanostructures-based gas sensors: a review, Energy Rep. 6 (2020) 46–62.
- [8] S.R. Ryu, S.D.G. Ram, H. Cho, D.J. Lee, T.W. Kang, Y. Woo, Single ZnO nanocactus gas sensor formed by etching of ZnO nanorod, Nanoscale 7 (2015) 11115–11122.
- [9] R. Kumar, O. Al-Dossary, G. Kumar, A. Umar, Zinc oxide nanostructures for NO 2 gas-sensor applications: a review, Nanomicro Lett. 7 (2015) 97–120.
- [10] O. Lupan, V. Postica, J. Gröttrup, A.K. Mishra, N.H. De Leeuw, J.F.C. Carreira, J. Rodrigues, N. Ben Sedrine, M.R. Correia, T. Monteiro, Hybridization of zinc oxide tetrapods for selective gas sensing applications, ACS. Appl. Mater. Interfaces. 9 (2017) 4084–4099.
- [11] F. Morisot, C. Zuliani, J. Luque, Z. Ali, M. Mouis, V.H. Nguyen, D. Muñoz-Rojas, O. Lourhzal, M. Texier, T.W. Cornelius, ZnO based nanowire network for gas sensing applications, Mater. Res. Express. 6 (2019) 084004.
- [12] J.-H. Kim, A. Mirzaei, H.W. Kim, S.S. Kim, Low power-consumption CO gas sensors based on Au-functionalized SnO2-ZnO core-shell nanowires, Sens. Actuators. B Chem. 267 (2018) 597–607.
- [13] J.Y. Son, S.J. Lim, J.H. Cho, W.K. Seong, H. Kim, Synthesis of horizontally aligned ZnO nanowires localized at terrace edges and application for high sensitivity gas sensor, Appl. Phys. Lett. 93 (2008) 053109.
- [14] V.S. Bhati, S. Ranwa, S. Rajamani, K. Kumari, R. Raliya, P. Biswas, M. Kumar, Improved sensitivity with low limit of detection of a hydrogen gas sensor based on rGO-loaded Ni-doped ZnO nanostructures, ACS. Appl. Mater. Interfaces. 10 (2018) 11116–11124.
- [15] O. Lupan, V.V. Ursaki, G. Chai, L. Chow, G.A. Emelchenko, I.M. Tiginyanu, A. N. Gruzintsev, A.N. Redkin, Selective hydrogen gas nanosensor using individual ZnO nanowire with fast response at room temperature, Sens. Actuators. B Chem. 144 (2010) 56–66.
- [16] P. Nakarungsee, S. Srirattanapibul, C. Issro, I.-M. Tang, S. Thongmee, High performance Cr doped ZnO by UV for NH3 gas sensor, Sens. Actuators Phys. 314 (2020) 112230.
- [17] J.-H. Kim, A. Mirzaei, H.W. Kim, P. Wu, S.S. Kim, Design of supersensitive and selective ZnO-nanofiber-based sensors for H2 gas sensing by electron-beam irradiation, Sens. Actuators. B Chem. 293 (2019) 210–223.
- [18] M.R. Waikar, P.M. Raste, R.K. Sonker, V. Gupta, M. Tomar, M.D. Shirsat, R. G. Sonkawade, Enhancement in NH3 sensing performance of ZnO thin-film via gamma-irradiation, J. Alloys. Compd. 830 (2020) 154641.
- [19] H.W. Kim, Y.J. Kwon, A. Mirzaei, S.Y. Kang, M.S. Choi, J.H. Bang, S.S. Kim, Synthesis of zinc oxide semiconductors-graphene nanocomposites by microwave irradiation for application to gas sensors, Sens. Actuators. B Chem. 249 (2017) 590–601.

- [20] L. Balakrishnan, S. Gokul Raj, S.R. Meher, K. Asokan, Z.C. Alex, Impact of 100 MeV Ag 7+ SHI irradiation fluence and N incorporation on structural, optical, electrical and gas sensing properties of ZnO thin films, Appl. Phys. A 119 (2015) 1541–1553.
- [21] K.Y. Shin, A. Mirzaei, W. Oum, D.J. Yu, S. Kang, E.B. Kim, H.M. Kim, S.S. Kim, H. W. Kim, Enhancement of selective NO2 gas sensing via xenon ion irradiation of ZnO nanoparticles, Sens. Actuators. B Chem. 374 (2023) 132808.
- [22] S.M. Majhi, A. Mirzaei, S. Navale, H.W. Kim, S.S. Kim, Boosting the sensing properties of resistive-based gas sensors by irradiation techniques: a review, Nanoscale 13 (2021) 4728–4757.
- [23] S.P. Bharath, K.V. Bangera, G.K. Shivakumar, Properties of CdxZn1-xO thin films and their enhanced gas sensing performance, J. Alloys. Compd. 720 (2017) 39–46.
- [24] T.T. Suzuki, T. Ohgaki, Y. Adachi, I. Sakaguchi, M. Nakamura, H. Ohashi, A. Aimi, K. Fujimoto, Ethanol gas sensing by a Zn-terminated ZnO (0001) bulk single-crystalline substrate, ACS. Omega 5 (2020) 21104–21112.
- [25] S. Bhatia, N. Verma, R.K. Bedi, Ethanol gas sensor based upon ZnO nanoparticles prepared by different techniques, Results. Phys. 7 (2017) 801–806.
- [26] J.Y. Patil, A.V. Rajgure, L.K. Bagal, R.C. Pawar, I.S. Mulla, S.S. Suryavanshi, Structural, morphological, and gas response properties of citrate gel synthesized nanocrystalline ZnO and ZnO. 9CdO, 1O Mater. Ceram. Int. 39 (2013) 4383–4390.
- [27] Y.-H. Liu, S.-J. Young, L.-W. Ji, Y.-L. Chu, S.-J. Chang, High-sensitive ethanol gas sensor using Ag modified ZnO nanosheets, Talanta Open. 10 (2024) 100386.
- [28] L. Zhu, Y. Li, W. Zeng, Hydrothermal synthesis of hierarchical flower-like ZnO nanostructure and its enhanced ethanol gas-sensing properties, Appl. Surf. Sci. 427 (2018) 281–287.
- [29] X. Deng, L. Zhang, J. Guo, Q. Chen, J. Ma, ZnO enhanced NiO-based gas sensors towards ethanol, Mater. Res. Bull. 90 (2017) 170–174.
- [30] S. Zhao, Y. Shen, F. Hao, C. Kang, B. Cui, D. Wei, F. Meng, Pn junctions based on CuO-decorated ZnO nanowires for ethanol sensing application, Appl. Surf. Sci. 538 (2021) 148140.
- [31] A. Umar, M.A. Khan, R. Kumar, H. Algarni, Ag-doped ZnO nanoparticles for enhanced ethanol gas sensing application, J. Nanosci. Nanotechnol. 18 (2018) 3557–3562.
- [32] H.R. Yousefi, B. Hashemi, A. Mirzaei, H. Roshan, M.H. Sheikhi, Effect of Ag on the ZnO nanoparticles properties as an ethanol vapor sensor, Mater. Sci. Semicond. Process. 117 (2020) 105172.
- [33] Y. Wei, X. Wang, G. Yi, L. Zhou, J. Cao, G. Sun, Z. Chen, H. Bala, Z. Zhang, Hydrothermal synthesis of Ag modified ZnO nanorods and their enhanced ethanolsensing properties, Mater. Sci. Semicond. Process. 75 (2018) 327–333.
- [34] M. Zajac, T. Giela, K. Freindl, K. Kollbek, J. Korecki, E. Madej, K. Pitala, A. Koziol-Rachwał, M. Sikora, N. Spiridis, The first experimental results from the 04BM (PEEM/XAS) beamline at Solaris, Nucl. Instrum. Methods Phys. Res. B 492 (2021) 43–48.
- [35] J. Szlachetko, J. Szade, E. Beyer, W. Błachucki, P. Ciochoń, P. Dumas, K. Freindl, G. Gazdowicz, S. Glatt, K. Guła, SOLARIS national synchrotron radiation centre in Krakow, Poland, Eur. Phys. J. Plus 138 (2023) 1–10.
- [36] B. Ravel, M. Newville, ARTEMIS ATHENA, HEPHAESTUS: data analysis for X-ray absorption spectroscopy using IFEFFIT, J. Synchrotron. Radiat. 12 (2005) 537–541
- [37] B. Meyer, First-principles study of the polar O-terminated ZnO surface in thermodynamic equilibrium with oxygen and hydrogen, Phys. Rev. B 69 (2004) 045416.
- [38] P.E. Blöchl, Projector augmented-wave method, Phys. Rev. B 50 (1994) 17953.
- [39] J.P. Perdew, M. Ernzerhof, K. Burke, Rationale for mixing exact exchange with density functional approximations, J. Chem. Phys. 105 (1996) 9982–9985.
- [40] M. Zhang, L. Qi, Tuning hydrogen adsorption on pure and doped ZnO (0001⁻) surfaces by a simple electron counting model, J. Appl. Phys. 124 (2018).
- [41] W. Jia, S. Dang, H. Liu, Z. Zhang, C. Yu, X. Liu, B. Xu, Evidence of the formation mechanism of ZnO in aqueous solution, Mater. Lett. 82 (2012) 99–101.
- [42] M. Alzaid, W.S. Mohamed, R. Alanazi, I.H. Alsohaimi, H.M.A. Hassan, N.M. A. Hadia, M. Ezzeldien, M.R. El-Aassar, A.M. Abu-Dief, Novel (Y2O3) x (CdO) 1-x binary mixed oxide nanocomposites: facile synthesis, characterization, and photocatalysis enhancement. J. Mater. Res. Technol. 23 (2023) 2454–2466.
- [43] N. Gautam, F. Singh, S.K. Gautam, R.G. Singh, S. Ojha, A. Kapoor, Growth of highly transparent CdxZn1-xO (CZO) thin films: structural and optical studies, J. Alloys. Compd. 650 (2015) 311–317, https://doi.org/10.1016/j.jallcom.2015.07.283.
- [44] H. Kumar, A. Tripathi, A.B. Dey, M. Gupta, R. Krishna, D.K. Avasthi, Improved hydrogen sensing behaviour in ion-irradiated Pd-Au alloy thin films, Sens. Actuators. B Chem. 301 (2019) 127006.
- [45] A. Katoch, G.-J. Sun, S.-W. Choi, J.-H. Byun, S.S. Kim, Competitive influence of grain size and crystallinity on gas sensing performances of ZnO nanofibers, Sens. Actuators. B Chem. 185 (2013) 411–416.
- [46] J.Y. Park, K. Asokan, S.-W. Choi, S.S. Kim, Growth kinetics of nanograins in SnO2 fibers and size dependent sensing properties, Sens. Actuators. B Chem. 152 (2011) 254–260.
- [47] Q.A. Drmosh, Z.H. Yamani, M.K. Hossain, Hydrogen gas sensing performance of low partial oxygen-mediated nanostructured zinc oxide thin film, Sens. Actuators. B Chem. 248 (2017) 868–877.
- [48] A. Das, D. Singh, C.P. Saini, R. Ahuja, A. Kaur, S. Aliukov, Orbital hybridizationinduced band offset phenomena in Ni x Cd 1 – x O thin films, Nanoscale 12 (2020) 669–686.
- [49] A. Das, C.P. Saini, D. Singh, R. Ahuja, A. Kaur, S. Aliukov, D. Shukla, F. Singh, High temperature-mediated rocksalt to wurtzite phase transformation in cadmium oxide nanosheets and its theoretical evidence, Nanoscale 11 (2019) 14802–14819.
- [50] L.F.J. Piper, P.H. Jefferson, T.D. Veal, C.F. McConville, J. Zuñiga-Pérez, V. Munoz-Sanjosé, X-ray photoemission studies of the electronic structure of single-crystalline CdO (100), Superlattices. Microstruct. 42 (2007) 197–200.

- [51] E.-J. Yun, J.W. Jung, K.N. Ko, J. Hwang, B.C. Lee, M.-H. Jung, Effect of high-energy electron beam irradiation on the properties of AZO thin films prepared by rf magnetron sputtering, Thin. Solid. Films. 518 (2010) 6236–6240.
- [52] S. Sabine-A, B. Giulio, P. Lorenzo, B. Rafael, D. Claudia, C. Thomas, C.M. Benedetta, Fingerprint of fractional charge transfer at the metal/organic interface, (2015).
- [53] F. Meng, F. Ge, Y. Chen, G. Xu, F. Huang, Local structural changes induced by ion bombardment in magnetron sputtered ZnO: al films: raman, XPS, and XAS study, Surf. Coat. Technol. 365 (2019) 2–9.
- [54] Y. Tu, S. Chen, X. Li, J. Gorbaciova, W.P. Gillin, S. Krause, J. Briscoe, Control of oxygen vacancies in ZnO nanorods by annealing and their influence on ZnO/ PEDOT: PSS diode behaviour, J. Mater. Chem. C. Mater. 6 (2018) 1815–1821.
- [55] F.-M. Chang, S. Brahma, J.-H. Huang, Z.-Z. Wu, K.-Y. Lo, Strong correlation between optical properties and mechanism in deficiency of normalized selfassembly ZnO nanorods, Sci. Rep. 9 (2019) 905.
- [56] R. Dutta, N. Mandal, Mg doping in wurtzite ZnO coupled with native point defects: a mechanism for enhanced n-type conductivity and photoluminescence, Appl. Phys. Lett. 101 (2012) 042106.
- [57] S. Lany, A. Zunger, Dopability, intrinsic conductivity, and nonstoichiometry of transparent conducting oxides, Phys. Rev. Lett. 98 (2007) 045501.
- [58] J.W. Chiou, K.P.K. Kumar, J.C. Jan, H.M. Tsai, C.W. Bao, W.-F. Pong, F.Z. Chien, M.-H. Tsai, I.-H. Hong, R. Klauser, Diameter dependence of the electronic structure of ZnO nanorods determined by x-ray absorption spectroscopy and scanning photoelectron microscopy, Appl. Phys. Lett. 85 (2004) 3220–3222.
- [59] H.S. Hsu, J.-C.A. Huang, Y.H. Huang, Y.F. Liao, M.Z. Lin, C.H. Lee, J.F. Lee, S. F. Chen, L.Y. Lai, C.-P. Liu, Evidence of oxygen vacancy enhanced room-temperature ferromagnetism in Co-doped ZnO, Appl. Phys. Lett. 88 (2006) 242507.
- [60] K. Lorenz, E. Alves, E. Wendler, O. Bilani, W. Wesch, M. Hayes, Damage formation and annealing at low temperatures in ion implanted ZnO, Appl. Phys. Lett. 87 (2005) 191904.
- [61] C. Guglieri, E. Céspedes, C. Prieto, J. Chaboy, X-ray absorption study of the local order around Mn in Mn: znO thin films: the role of vacancies and structural distortions, J. Phys.: Condens. Matter 23 (2011) 206006.
- [62] V. Kumar, A. Bhogra, M. Bala, S.C. Haw, C.L. Chen, C.L. Dong, K. Asokan, S. Annapoorni, Origin of intense blue-green emission in Sr Ti O 3 thin films with implanted nitrogen ions: an investigation by synchrotron-based experimental techniques, Phys. Rev. B 103 (2021) 024104.
- [63] A. López-Suárez, D. Acosta, C. Magaña, Effect of 4He2+ ion irradiation on the optical, electrical, morphological, and structural properties of ZnO thin films, Mater. Res. Express. 9 (2022) 116403.
- [64] S. Lv, M. Li, M. Qiu, Y. Wang, F. Dong, C. Chen, J. Cheng, Z. Li, Effect of nitrogen ion irradiation treatment to the enhancement of ZnO photocatalytic performance, Surf. Interface Anal. 52 (2020) 348–354.
- [65] S. Krishnamurthy, C. McGuinness, L.S. Dorneles, M. Venkatesan, J.M.D. Coey, J. G. Lunney, C.H. Patterson, K.E. Smith, T. Learmonth, P.-A. Glans, Soft-x-ray spectroscopic investigation of ferromagnetic Co-doped ZnO, J. Appl. Phys. 99 (2006) 08M111.
- [66] I.N. Demchenko, M. Chernyshova, T. Tyliszczak, J.D. Denlinger, K.M. Yu, D. T. Speaks, O. Hemmers, W. Walukiewicz, G. Derkachov, K. Lawniczak-Jablonska, Electronic structure of CdO studied by soft X-ray spectroscopy, J. Electron. Spectros Relat. Phenom. 184 (2011) 249–253.
- [67] H. Zhao, Y. Li, L. Yang, X. Wu, Synthesis, characterization and gas-sensing property for C2H5OH of SnO2 nanorods, Mater. Chem. Phys. 112 (2008) 244–248.
- [68] S. Pati, P. Banerji, S.B. Majumder, Properties of indium doped nanocrystalline ZnO thin films and their enhanced gas sensing performance, RSC. Adv. 5 (2015) 61230–61238.
- [69] N. Barsan, U. Weimar, Conduction model of metal oxide gas sensors, J. Electroceram. 7 (2001) 143–167.
- [70] M. Al-Hashem, S. Akbar, P. Morris, Role of oxygen vacancies in nanostructured metal-oxide gas sensors: a review, Sens. Actuators. B Chem. 301 (2019) 126845.
- [71] R. Xing, L. Xu, J. Song, C. Zhou, Q. Li, D. Liu, H.Wei Song, Preparation and gas sensing properties of In2O3/Au nanorods for detection of volatile organic compounds in exhaled breath, Sci. Rep. 5 (2015) 10717.
- [72] N. Illyaskutty, H. Kohler, T. Trautmann, M. Schwotzer, V.P.M. Pillai, Hydrogen and ethanol sensing properties of molybdenum oxide nanorods based thin films: effect of electrode metallization and humid ambience, Sens. Actuators. B Chem. 187 (2013) 611–621.
- [73] A.K. Prasad, D.J. Kubinski, P.-I. Gouma, Comparison of sol–gel and ion beam deposited MoO3 thin film gas sensors for selective ammonia detection, Sens. Actuators. B Chem. 93 (2003) 25–30.
- [74] V. Guidi, D. Boscarino, L. Casarotto, E. Comini, M. Ferroni, G. Martinelli, G. Sberveglieri, Nanosized Ti-doped MoO3 thin films for gas-sensing application, Sens. Actuators. B Chem. 77 (2001) 555–560.
- [75] S. Matsushima, T. Maekawa, J. Tamaki, N. Miura, N. Yamazoe, Role of additives on alcohol sensing by semiconductor gas sensor, Chem. Lett. 18 (1989) 845–848.
- [76] T.T. Suzuki, T. Ohgaki, Y. Adachi, I. Sakaguchi, M. Nakamura, H. Ohashi, A. Aimi, K. Fujimoto, Ethanol gas sensing by a Zn-terminated ZnO (0001) bulk singlecrystalline substrate, ACS. Omega 5 (2020) 21104–21112.
- [77] N. Illyaskutty, H. Kohler, T. Trautmann, M. Schwotzer, V.P.M. Pillai, Hydrogen and ethanol sensing properties of molybdenum oxide nanorods based thin films: effect of electrode metallization and humid ambience, Sens. Actuators. B Chem. 187 (2013) 611–621.
- [78] S. De, N. Venkataramani, S. Prasad, R.O. Dusane, L. Presmanes, Y. Thimont, P. Tailhades, V. Baco-Carles, C. Bonningue, S.T. Pisharam, Ethanol and hydrogen gas-sensing properties of CuO-CuFe 2 O 4 nanostructured thin films, IEEE Sens. J. 18 (2018) 6937–6945.

- [79] M. Tonezzer, T.T. Le Dang, Q.H. Tran, S. Iannotta, Dual-selective hydrogen and ethanol sensor for steam reforming systems, Sens. Actuators. B Chem. 236 (2016) 1011–1019.
- [80] R. Schaub, P. Thostrup, N. Lopez, E. Lægsgaard, I. Stensgaard, J.K. Nørskov, F. Besenbacher, Oxygen vacancies as active sites for water dissociation on rutile TiO 2 (110), Phys. Rev. Lett. 87 (2001) 266104.
- [81] C. Zhang, G. Liu, X. Geng, K. Wu, M. Debliquy, Metal oxide semiconductors with highly concentrated oxygen vacancies for gas sensing materials: a review, Sens. Actuators Phys. 309 (2020) 112026.
- [82] G. Korotcenkov, B.K. Cho, Metal oxide composites in conductometric gas sensors: achievements and challenges, Sens. Actuators. B Chem. 244 (2017) 182–210.
- [83] T. Minezaki, P. Krüger, F.E. Annanouch, J. Casanova-Cháfer, A. Alagh, I.J. Villar-Garcia, V. Pérez-Dieste, E. Llobet, C. Bittencourt, Hydrogen sensing mechanism of WS2 gas sensors analyzed with DFT and NAP-XPS, Sensors 23 (2023) 4623.
- [84] F.A. Kröger, H.J. Vink, Relations between the concentrations of imperfections in crystalline solids, Solid State Phys. 3 (1956) 307–435.

- [85] Y. Yan, M.M. Al-Jassim, S.-H. Wei, Oxygen-vacancy mediated adsorption and reactions of molecular oxygen on the ZnO (10 1 0) surface, Phys. Rev. B 72 (2005) 161307.
- [86] R. Haul, D. Just, Disorder and oxygen transport in cadmium oxide, J. Appl. Phys. 33 (1962) 487–493.
- [87] Y. Wang, M. Chen, Y. Li, Q. Du, Y. Yuan, Y. Ren, B. Liu, H. Zhao, H. Yang, Enhancing gas sensitivity of CdO octahedrons having {111} facets by hydrogenation and sensing mechanism of 3-coordinated Cd atoms as the reactive centers, Appl. Surf. Sci. 506 (2020) 144868.
- [88] Y.-Q. Zhang, Z. Li, T. Ling, S.A. Kulinich, X.-W. Du, Superior gas-sensing performance of amorphous CdO nanoflake arrays prepared at room temperature, J. Mater. Chem. Mater. 4 (2016) 8700–8706.
- [89] R.N. Bulakhe, C.D. Lokhande, Chemically deposited cubic structured CdO thin films: use in liquefied petroleum gas sensor, Sens. Actuators. B Chem. 200 (2014) 245–250